

GlueX FDIRC Technical Design Report

(The GLUEX Collaboration)

(Dated: September 30, 2015)

We propose to enhance the kaon identification capabilities of the GLUEX detector by constructing an FDIRC (Focusing Detection of Internally Reflected Cherenkov) detector utilizing the decommissioned BaBar DIRC components. The GLUEX FDIRC will significantly enhance the GLUEX physics program by allowing one to search for and study hybrid mesons decaying into kaon final states. Such systematic studies of kaon final states are essential for inferring the quark flavor content of hybrid and conventional mesons. The GLUEX FDIRC will reuse one-third of the synthetic fused silica bars that were utilized in the BaBar DIRC. A new focussing photon camera, read out with MaPMTs, is being developed. We propose operating the enhanced GLUEX detector in Hall D for a total of 220 days at an average intensity of $5 \times 10^7 \gamma/\text{s}$, a program that was approved by PAC42.

CONTENTS

I. Introduction	4
II. Requirements	6
III. FDIRC Design	9
A. Introduction and Overview	9
B. Simulation	15
C. Reconstruction Algorithms	18
D. Optimization and Requirements	20
E. EM Background	26
F. Effects of the FDIRC on other GLUEX Systems	27
IV. Focusing Box Design	29
A. Mirrors	29
B. Box Design	37
V. Photon Detection and Readout	40
A. Introduction and Requirements	40
B. Multi-Anode Photomultipliers	41
C. Electronics	43
VI. Mechanical Design, Integration and Installation	47
VII. Transport to JLab	50
VIII. First Article Validation Plans	55
IX. Project Details	57
A. Institutional contributions	57
X. Summary	58
A. Letter from BaBar Reuse Committee	59
B. Summary of reviews by Jefferson Lab's Program Advisory Committee	63

C. Report from Jefferson Lab's 42 nd Program Advisory Committee	64
References	65

I. INTRODUCTION

The GlueX experiment will provide the data necessary to construct quantitative tests of non-perturbative QCD by studying the spectrum of light-quark mesons and baryons. The primary goal of the GlueX experiment is to search for and study the spectrum of so-called hybrid mesons that are formed by exciting the gluonic field that couples the quarks. QCD-based calculations predict the existence of hybrid meson states, including several that have exotic quantum numbers that cannot be formed from a simple quark/anti-quark pair. To achieve its goal, GlueX must systematically study all possible decay modes of conventional and hybrid mesons, including those with kaons. The addition of a Cherenkov-based particle identification (PID) system utilizing the BaBar DIRC (Detection of Internally Reflected Cherenkov) components will dramatically increase the number of potential hybrid decay modes that GlueX can access, and will reduce the experimental backgrounds from misidentified particles in each mode. This enhanced capability will be crucial for the GlueX experiment to realize its full discovery potential.

The GlueX physics program was presented initially to the Jefferson Lab Program Advisory Committee (PAC) in 2006 [28]. The first beam time allocations were made for the commissioning phases of GlueX after presentation to the PAC in 2010 [29]. This allocation covered phases I-III of the run plan highlighted in Table I. In 2013 the collaboration developed a PAC proposal for running at design intensity with limited PID capability [2]; this was approved by the PAC and 200 days of beam for Phase IV were granted. Prior to this, the collaboration presented a proposal to the PAC in 2012 that would include then-undefined upgrades to the forward PID system. This was conditionally approved, but the PAC wanted to see a more concrete PID design [1]. In late 2013, the collaboration made a proposal to SLAC for reusing four of the BaBar DIRC bar boxes as the central element of a forward kaon-identification system in GlueX. This was approved in the late spring of 2014, and an update to the 2012 PAC proposal utilizing the BaBar DIRC as the particle-identification system was presented to the PAC [3]. This proposal included both the enhanced particle-identification capability as well as running at design intensity. The PAC approved this proposal for 220 days of running (noted as Phase IV+ in Table I), with the assumption that there would likely be very large overlaps in the approved running time of Phase IV and IV+.

The GlueX experiment is installed in Hall D at Jefferson Lab, and collected it's first commissioning beam in the Fall of 2014. A subsequent run in the Spring of 2015 allowed the experiment to start commissioning polarized photon beams, and to continue work on calibration of the detector.

More commissioning is expected in late 2015 and/or early 2016, with first physics data taking in late 2016. The collaboration consists of over a hundred members, including representation from the theory community.

In this document, we present our design for a DIRC-based forward PID system in GLUEX using components from the BaBar DIRC. Our plan is to pursue construction of this design on a time scale that allows us to merge both Phase IV and Phase IV+ into a single run.

TABLE I. A table of relevant parameters for the various phases of approved GLUEX running.

	Phase I	Phase II	Phase III	Phase IV	Phase IV+
Duration (PAC days)	30	30	60	200	220 ^a
Minimum electron energy (GeV)	10	11	12	12	12
Average photon flux (γ/s)	10^6	10^7	10^7	5×10^7	5×10^7
Level-one (hardware) trigger rate (kHz)	2	20	20	200	200
Raw Data Volume (TB) ^b	60	600	1200	2300	2300

^a Twenty days are allocated for FDIRC commissioning.

^b Phase IV(+) assumes a level-three software trigger is implemented.

II. REQUIREMENTS

A schematic view of the GLUEX detector is shown in Fig. 1. The GLUEX photon beam is derived from coherent bremsstrahlung radiation produced by the CEBAF electron beam scattering off of a thin diamond wafer. Downstream collimation removes the bulk of the lower energy photons produced. Proper orientation of the diamond, when combined with the collimation, leads to a photon energy spectrum that peaks around 9 GeV and is about 40% linearly polarized within the peak. The photon energy is tagged precisely in the coherent peak and coarsely over a broad range of photon energies. The photon beam is then incident on a liquid hydrogen target located inside of the GlueX detector.

Charged particles are tracked by a central cylindrical straw-tube drift chamber and four forward planar drift chambers, each of which is located within a 2 T superconducting solenoid. The solenoidal geometry has the benefit of reducing electromagnetic backgrounds in the detectors since low energy e^+e^- pairs spiral within a small radius of the beam line. The calorimetry system consists of a central barrel calorimeter and a forward planar lead-glass calorimeter. Identifying the beam bunch, which is critical for timing measurements, is performed by a thin start counter that surrounds the target.

The PID capabilities of GLUEX are derived from several subsystems. A dedicated forward time-of-flight wall, which is constructed from two planes of 2.5-cm-thick scintillator bars, was designed to provide about 70 ps timing resolution on forward-going tracks within about 10° of the beam axis. This information is complemented by time-of-flight data from the BCAL and specific ionization (dE/dx) measured with both drift-chamber systems, which are currently sufficient to identify recoil protons in $\gamma p \rightarrow X p$ reactions.

The GLUEX commissioning data collected in Spring 2015 provided a dataset to calibrate many of the detectors, including the forward time-of-flight which performed very close to its designed time resolution. Fig. 2 shows the measured β from the forward time-of-flight as a function of the charged track momentum, and preliminary measurements show that $K - \pi$ separation of 3σ has been achieved for momenta up to about 2 GeV/c . This level of separation is the result of several systems, so improving this using upgrades to current technologies requires improvements in several major detector systems. Thus, to improve the $K - \pi$ separation, we plan to add a DIRC-based PID system in the forward region in front of the time-of-flight wall. The design of this new system is presented in the following sections. In the remainder of this section, we define the DIRC

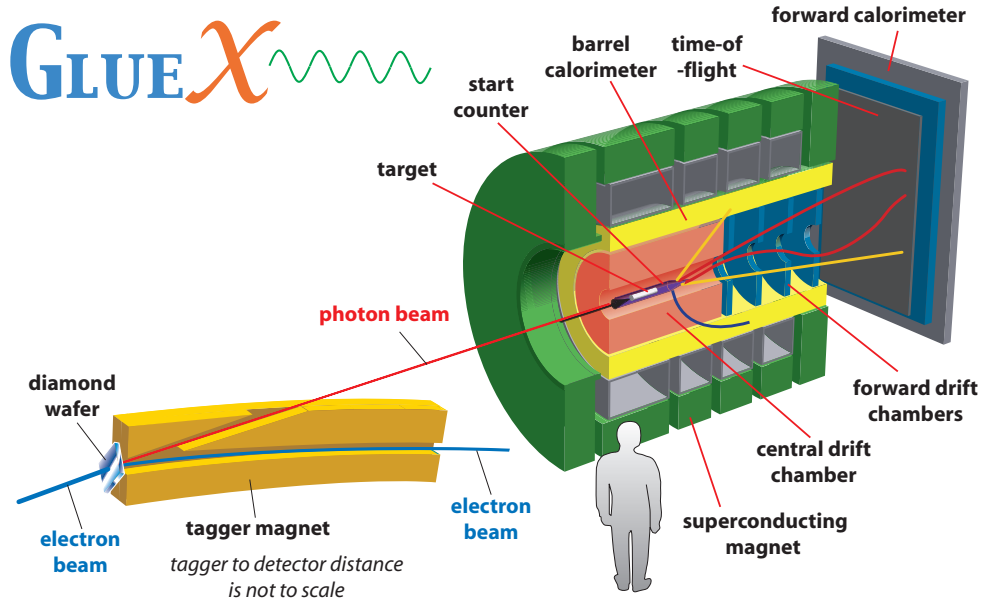


FIG. 1. A schematic of the baseline GLUEX detector and beam. The FDIRC will be installed in the open area in front of the time-of-flight wall.

performance requirements to satisfy the physics goals of GLUEX.

In Ref. [3] it was shown that achieving a resolution on the Cherenkov angle (θ_C) of $\lesssim 2.5$ mrad is critical for carrying out the full GLUEX physics program. The θ_C resolution has contributions from both the PID and tracking systems. The reconstructed track properties that impact the PID performance are the angle of incidence, the position, and the magnitude of the momentum of the particle as it enters the DIRC. To determine the resolution with which we can expect to measure these properties, we simulate charged pions originating in the target of the GLUEX detector produced uniformly in azimuth and covering the full forward acceptance of GLUEX, which is limited by the beam pipe and solenoid to $2 \lesssim \theta \lesssim 11^\circ$. A complete GEANT model is used to simulate the GLUEX detector response, and a Kalman Filter tracking algorithm is used to reconstruct the tracks. The reconstructed track helix is then extrapolated through the magnetic field to the plane of the DIRC detector. The resolution is shown in Fig. 3. We have studied how these tracking uncertainties propagate into uncertainties on θ_C using simulated kaons and pions. The uncertainty on the angle of incidence contributes $\lesssim 0.2$ mrad of uncertainty on θ_C . The position resolution is sufficient to contribute negligible uncertainty. Finally, the GLUEX momentum resolution contributes 0.1–0.5 mrad uncertainty on θ_C for particles with $p < 7$ GeV. In total, the GLUEX tracking system is

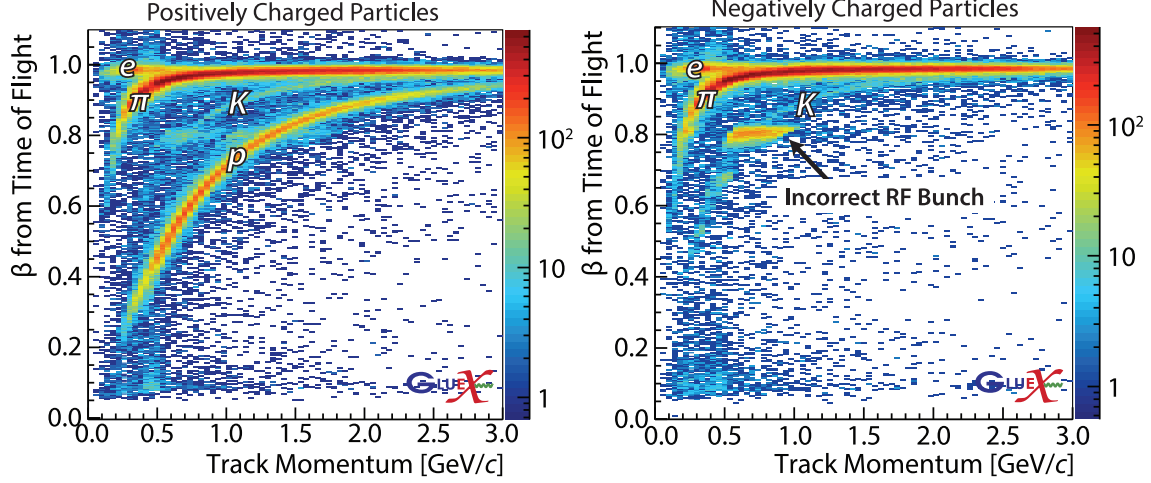


FIG. 2. Measured β from the forward time-of-flight as a function of charged track momentum from the Spring 2015 GLUEX commissioning data for positively charged particles (left) and negatively charged particles (right).

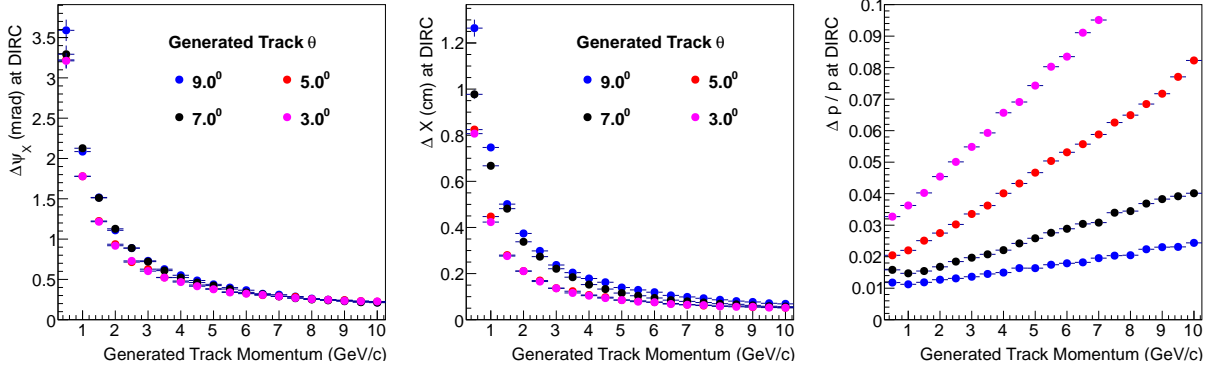


FIG. 3. Resolution on the track (left) angle of incidence, (middle) position and (right) momentum at the point of intersection with the DIRC. The resolution is approximately the same in all directions transverse to the beam line (denoted as the $x - y$ plane).

expected to contribute at most 0.5 mrad of uncertainty on θ_C for a 4 GeV particle. Therefore, the PID system must be able to provide a resolution of about 2.4 mrad – excluding the contribution from the tracking system – to achieve the necessary performance to achieve the physics goals.

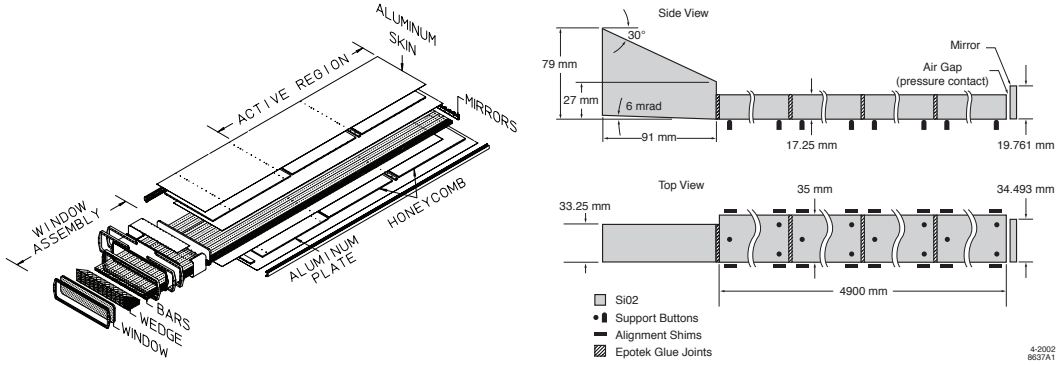


FIG. 4. Schematic diagram of one BaBar box showing the 12 quartz bars (4.9m long), mirror ends, wedges and window ends (left) and single radiator bar (right) [30].

III. FDIRC DESIGN

A. Introduction and Overview

The world's first DIRC detector was developed and utilized by the BaBar experiment. It provided excellent particle identification performance up to about 4 GeV/c [30]. The radiator of the BaBar DIRC consisted of a barrel made up of twelve boxes each containing twelve synthetic fused silica bars (in this document, we will refer to synthetic fused silica as quartz for the sake of brevity; however, it is worth noting that quartz is birefringent and, therefore, not suitable for use in the DIRC). Quartz was chosen because of the following properties of the material: it has a large index of refraction (n) and a small chromatic dispersion; it has a long attenuation length; it is highly resistant to ionizing radiation; and it is possible to polish its surface. Each box is hermetically sealed and nitrogen gas constantly flows through the box to prevent surface pollution and photon losses.

Figure 4 shows the assembly of one DIRC box. Each bar is 17.25 mm thick, 35 mm wide and 4.9 m long, and was produced by glueing four smaller bars end-to-end. One end of each box was coupled to a volume instrumented with photodetectors (the photon camera), while the other end has a mirror that reflects light back to the readout side. The readout side also has a quartz wedge glued to it. Neighboring bars are optically isolated by a 0.15 mm gap created using aluminum shims.

The quartz bars are used both as radiators and as light guides for the Cherenkov light trapped in the bars by total internal reflection. The number of photons produced is proportional to $1/\lambda^2$;

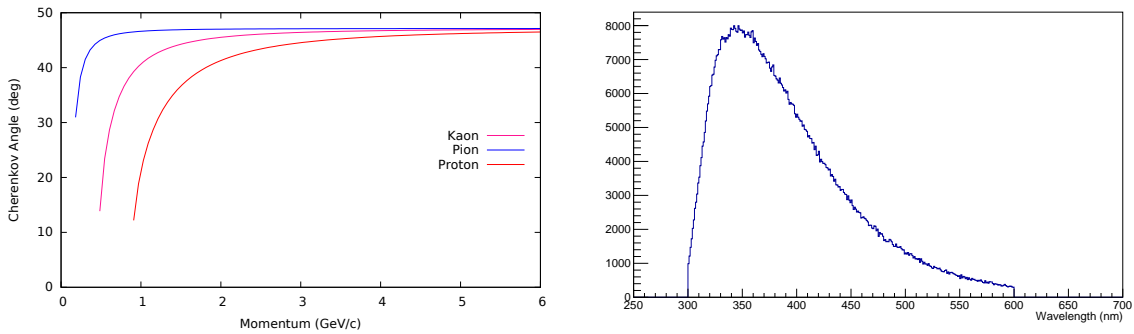


FIG. 5. (left) Cherenkov angle as a function of the momentum, for a fixed $n = 1.473$. (right) Reconstructed wavelength distribution of photons obtained by multiplying the PMT quantum efficiency by the quartz transmission efficiency and by the produced wavelength distribution.

however, the glue joints in the bars effectively filter out photons with $\lambda < 300$ nm. Furthermore, the quantum efficiency of PMTs peaks near blue light which also affects the reconstructed photon wavelength spectrum. The large index of refraction of the quartz material leads to a large number of Cherenkov photons produced within the wavelength acceptance of the DIRC (300-600 nm).

The Cherenkov light produced by a particle is emitted at an angle with respect to the direction of the particle's velocity, referred to as the Cherenkov angle (θ_C), given by

$$\cos \theta_C = \frac{1}{\beta n(\lambda)}.$$

The wavelength dependence of the index of refraction causes θ_C to be a function of λ . Figure 5 shows the Cherenkov angle for different particle types. One can see that for the average quartz index of refraction, $\langle n \rangle = 1.473$, the maximal Cherenkov angle is about 47° . The critical angle for trapping light via total internal reflection at the quartz-nitrogen boundary, given by the ratio of the indices of refraction, is $\theta_{\text{critical}} \approx 42.7^\circ$; therefore, $\theta_C > \theta_{\text{critical}}$ over most of the momentum range of interest for all particle types. An example of the path followed by a single photon trapped within a bar is shown in Fig. 6. The Cherenkov angle is preserved as the photon travels through the bar to the photodetectors.

The initial photon camera of the BaBar DIRC detector was very large and filled with 6000 liters of purified water. The design was updated for the SuperB experiment¹ to include focusing mirrors that permit detecting the Cherenkov light produced in the quartz radiator using a much more

¹ SuperB was designed to be the successor to BaBar but was canceled in 2012.

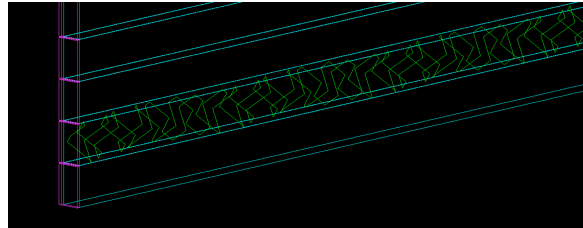


FIG. 6. A single photon bouncing within a bar. If the photon angle is larger than the critical angle, the light is internally reflected and the Cherenkov angle is preserved as the photon travels through the bar.

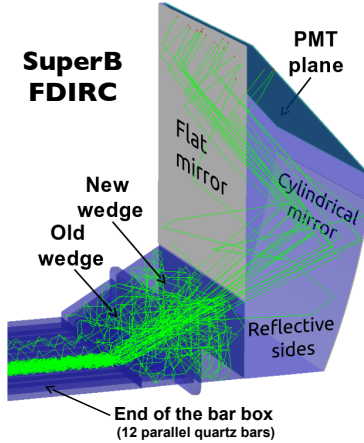


FIG. 7. SuperB FDIRC design (taken from Ref. [36]).

compact design [31–35]. The focusing DIRC (FDIRC) was designed at SLAC with the constraint that the BaBar boxes cannot be altered [36]. The updated photon camera system is about 25 times smaller than the camera used at BaBar yet has approximately the same Cherenkov angle resolution. The focusing design has the following advantages: the background rate is lower; the thickness of the bars can be corrected for; and the total number of photo-multipliers required is greatly reduced.

Figure 7 shows the focusing scheme of the FDIRC prototype developed at SLAC [36]. The photon camera consists of a new quartz wedge and a focusing quartz block. The block consists of a cylindrical mirror along with flat mirrors to focus the light onto the PMT plane. The cylindrical mirror removes the effect of the bar thickness on the Cherenkov angle resolution, since parallel rays are focused onto the same point on the photomultiplier (PMT) plane. The flat mirror then reflects the light almost perpendicularly to the detector plane.

The GLUEX detector geometry is quite different than BaBar or SuperB. The B-factory experiments configured the DIRC in a barrel and required good performance over a wide range of track entrance angles to the bars. GLUEX plans to orient the bars in a single plane in the forward region. This will result in charged particles entering the bars at near perpendicular angles. Figure 8 shows the proposed layout for the GLUEX FDIRC detector. The acceptance in the forward region of GLUEX is limited by the solenoid at $\lesssim 11^\circ$; therefore, to fully cover the acceptance requires four BaBar boxes, each containing 12 quartz bars. The bar boxes will be oriented horizontally in the GLUEX hall and placed symmetrically around the beam line. The FDIRC detector will fit into the reserved space between the downstream end of the GLUEX detector solenoid and the time-of-flight wall.

The planar alignment of the bar boxes permits using a common readout system for multiple BaBar boxes. Figure 9 shows a schematic of the optics for the proposed focusing box. Each focusing box will be filled with distilled water, whose index of refraction closely matches that of quartz. Figure 10 shows the occupancy in the PMT plane for charged particles thrown perpendicularly to a bar for both the SuperB and GLUEX design with a single focusing box for all four BaBar boxes. In the SuperB design, the pattern is folded onto itself due to reflections off of the side of the focusing block. The GLUEX design is able to remove these and, therefore, remove the possibility of ambiguities in the reconstruction due to photons emitted at different angles hitting the PMT plane in the same location. The baseline design for the GLUEX FDIRC is to use two separate focusing boxes which will each provide readout for two of the BaBar boxes, see Fig 8 a) and b). In practice, such ambiguities are removed using timing information; however, visualizing this requires making 3-dimensional plots. Instead, we choose to show the occupancy on the PMT plane throughout this report for a single focusing box design option, see Fig. 8 c), as this is easier to interpret. The only difference in performance between the two designs is a loss of photons of order 1% due to reflections off of the side mirrors in the two-box design.

Figure 11 shows the photon position in the photodetector plane as a function of the photon time of propagation (TOP), where TOP is defined as the time between a given photon's production in the quartz and its detection in the photodetector plane. The two bunches separated in time correspond to forward and backward emitted photons. The forward photons go directly from the creation point to the readout side, while the backward photons are reflected by the mirrors and then traverse the entire length of the bar. With the bars centered with respect to the beam line, the forward photons begin to arrive about 20 ns after production, making hundreds of bounces inside of the bars. The

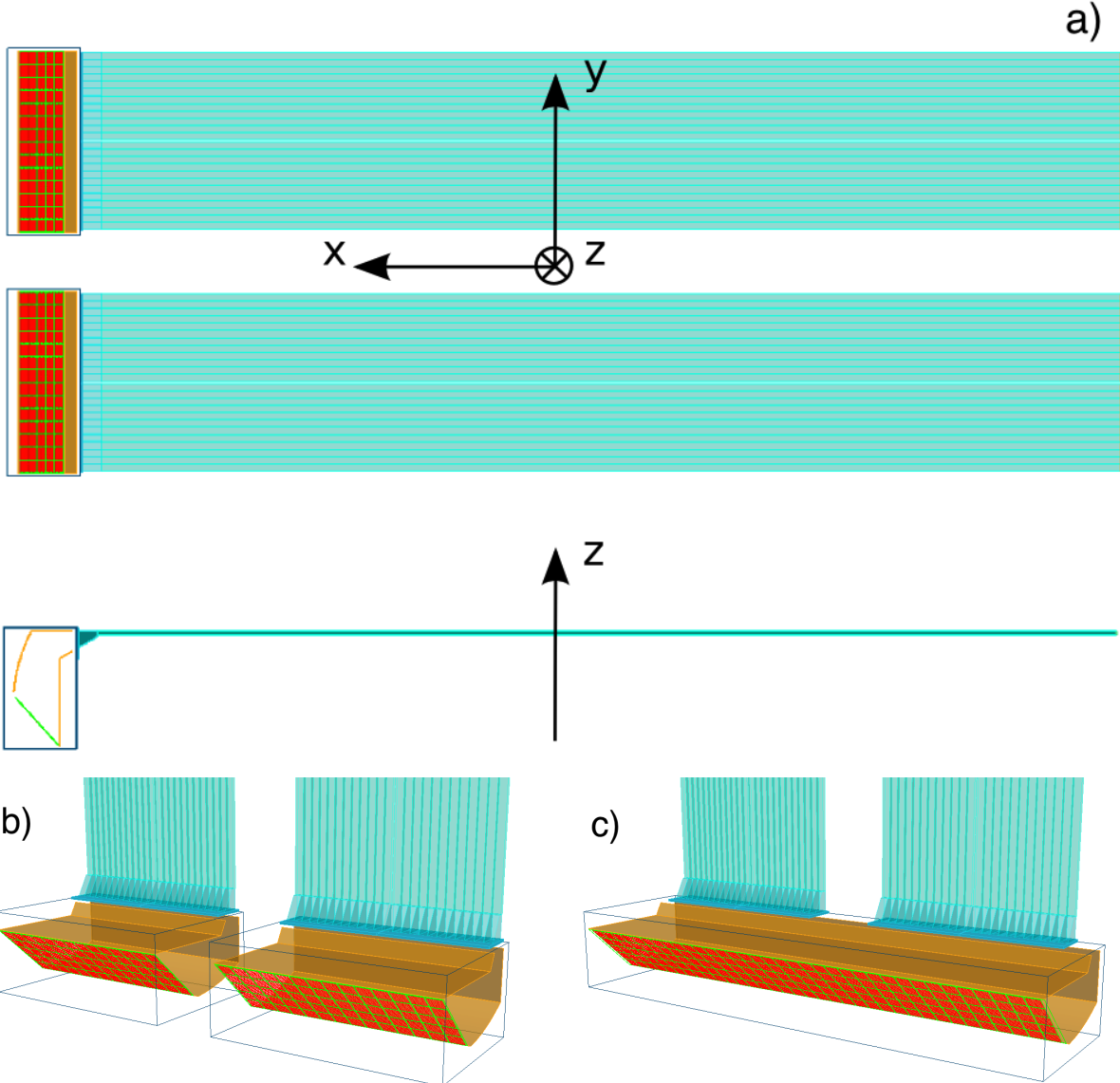


FIG. 8. a) Schematic diagram of the GLUEX FDIRC detector as implemented in GEANT4. Four BaBar boxes are required to cover the full acceptance. The bars are oriented horizontally. The beam line is along the \hat{z} direction and at $(x, y) = (0, 0)$. The bottom figures show b) the baseline design of two focusing boxes which each connect to two BaBar boxes and c) the design option to use a single focusing box for all four BaBar boxes.

backward photons travel about three times the path length. The large number of bounces made by the photons requires that the bars have excellent surface quality in order to preserve the Cherenkov angle. The position of the bars in the horizontal direction has not yet been optimized. There

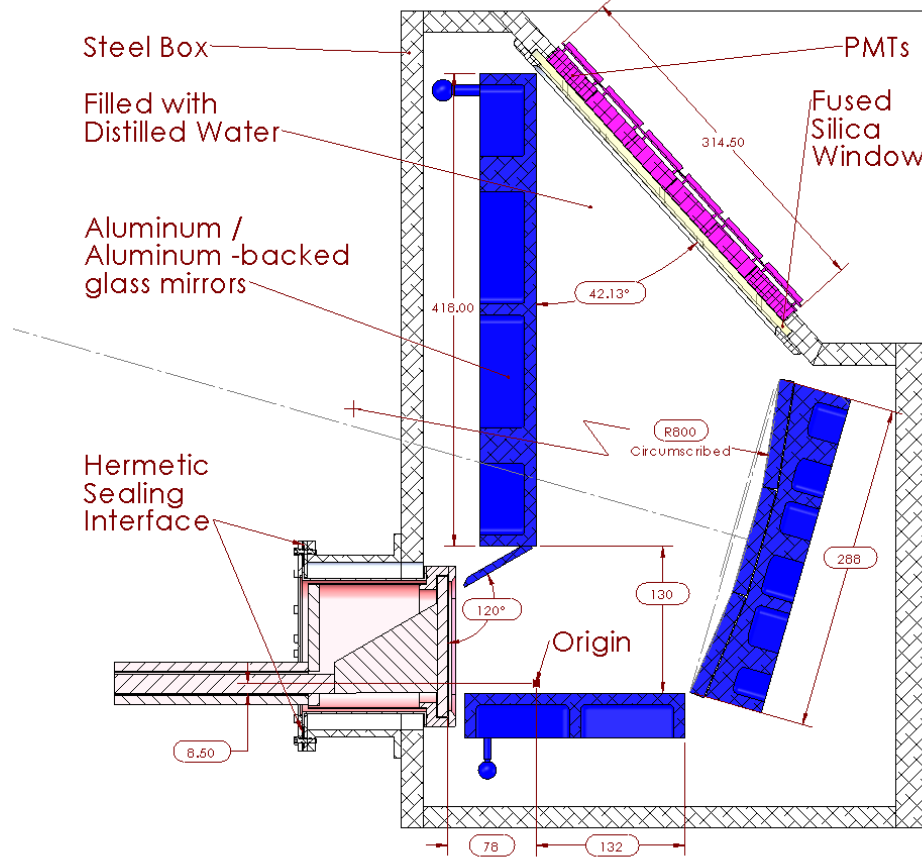


FIG. 9. Schematic diagram of the focusing box.

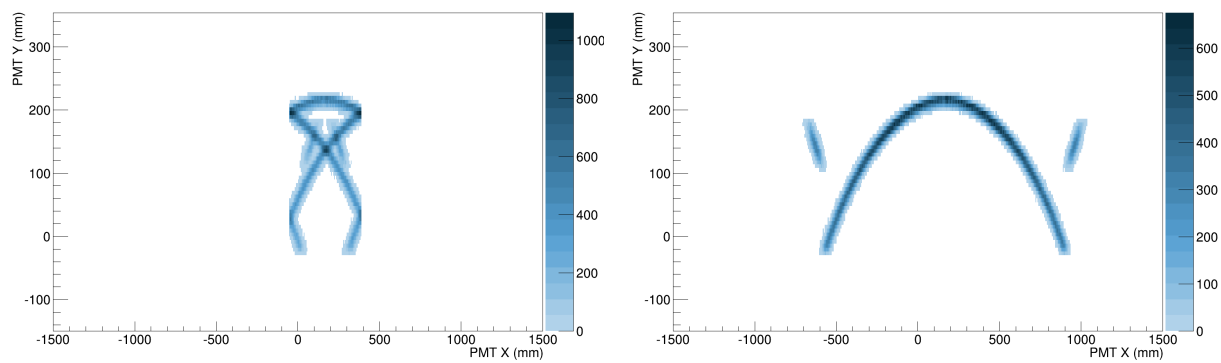


FIG. 10. Occupancy on the photodetector plane for a charged particle hitting a bar perpendicularly for the (left) SLAC design and (right) GLUEX single focusing box design option using an identical optical system design as SLAC. The number of photons corresponds to roughly 150k charged particles.

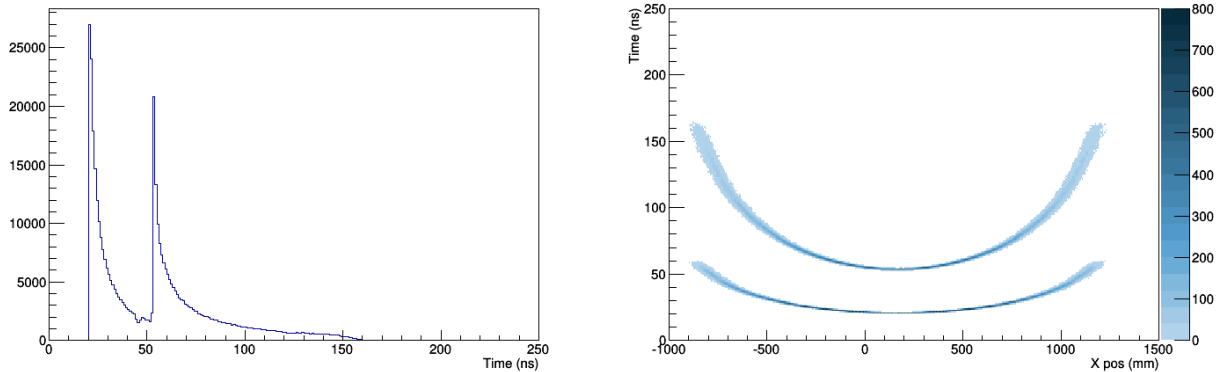


FIG. 11. (left) Cherenkov photon time of propagation (right) and time of propagation *vs* local position of the photon on the PMT plane.

is some freedom in their placement along this axis. We are studying how the placement of the bars along the horizontal axis affects the chromatic correction and other aspects of the FDIRC performance. For the rest of this section, we assume that the bars are centered relative to the beam line.

B. Simulation

The studies presented below are based on a fast simulation that has been extensively cross-checked using GEANT simulated events. The fast simulation has also been validated by comparing to the results obtained by SLAC on their FDIRC prototype [36]. The following provides an outline of how the fast simulation works:

- A charged particle is propagated through a DIRC bar on a given trajectory and at a fixed entry location. The initial position and trajectory are taken as inputs to the simulation. Multiple scattering of the particle as it travels through the bar is simulated by treating the bar as a large number of small segments (the results show negligible dependence on the number of segments provided it is greater than 10). After exiting each segment, the trajectory is augmented using the full Moliere scattering theory, which includes the Rutherford (non-Gaussian) tails.
- Cherenkov photons are emitted randomly along the particle's path through the bar. This automatically accounts for the effect on the resolution on θ_C due to the thickness of the bars.

- The λ spectrum generated is the product of the $1/\lambda^2$ production spectrum with the expected transmission and detection efficiency. The number of photons emitted per particle is determined by matching the distribution of detected photons to that observed by SLAC in their prototype, then accounting for the differences expected in our design (discussed below). Since the quantum efficiency and active area of the PMTs, along with photon losses in the bars and focusing box, are included in the generated spectrum and in the normalization, any photon that reaches the PMT plane is taken to have perfect detection efficiency. This approach avoids tracing a large number of photons through the bars and optical system that end up not being reconstructed.
- The value of θ_C for each photon is determined by the particle type and by λ .
- Each photon is analytically traced through the bars. The rectangular shape of the bars is accounted for here. Upon exiting the bars, the photon direction is smeared using a Gaussian distribution with $\sigma = 3 \text{ mrad}$ to account for distortion during transport along the bars [36].
- The wedge with an inclined surface attached as part of the BaBar design (which cannot be removed) is included in the simulation.
- The photons are analytically traced through the focusing system to the PMT plane. The mirrors are assumed to contribute negligible distortion to the reflected photon angle. The PMT pixel size is taken to be $6 \times 6 \text{ mm}^2$. The timing resolution of the PMT and readout electronics is taken to be 1 ns (see Sec. V A).

The only smearing applied is due to transport along the bars. All other effects that impact the resolution on θ_C are fully simulated. For example, Fig. 12 shows the so-called kaleidoscope effect which was first observed in the first SLAC FDIRC prototype.

The normalization of the number of photons expected is estimated using the published distribution of expected photon yield for nearly perpendicular tracks in the SLAC FDIRC prototype [36]. First, we configure our simulation to match the SLAC FDIRC design and fix the mean and width of the photon yield such that our reconstructed yield distribution matches Fig. 13(c) of Ref. [36] for perpendicular tracks. To scale this for GLUEX, the following differences must be accounted for:

- Attenuation of photons in 64 cm of water which results in a loss of about 5% of photons.

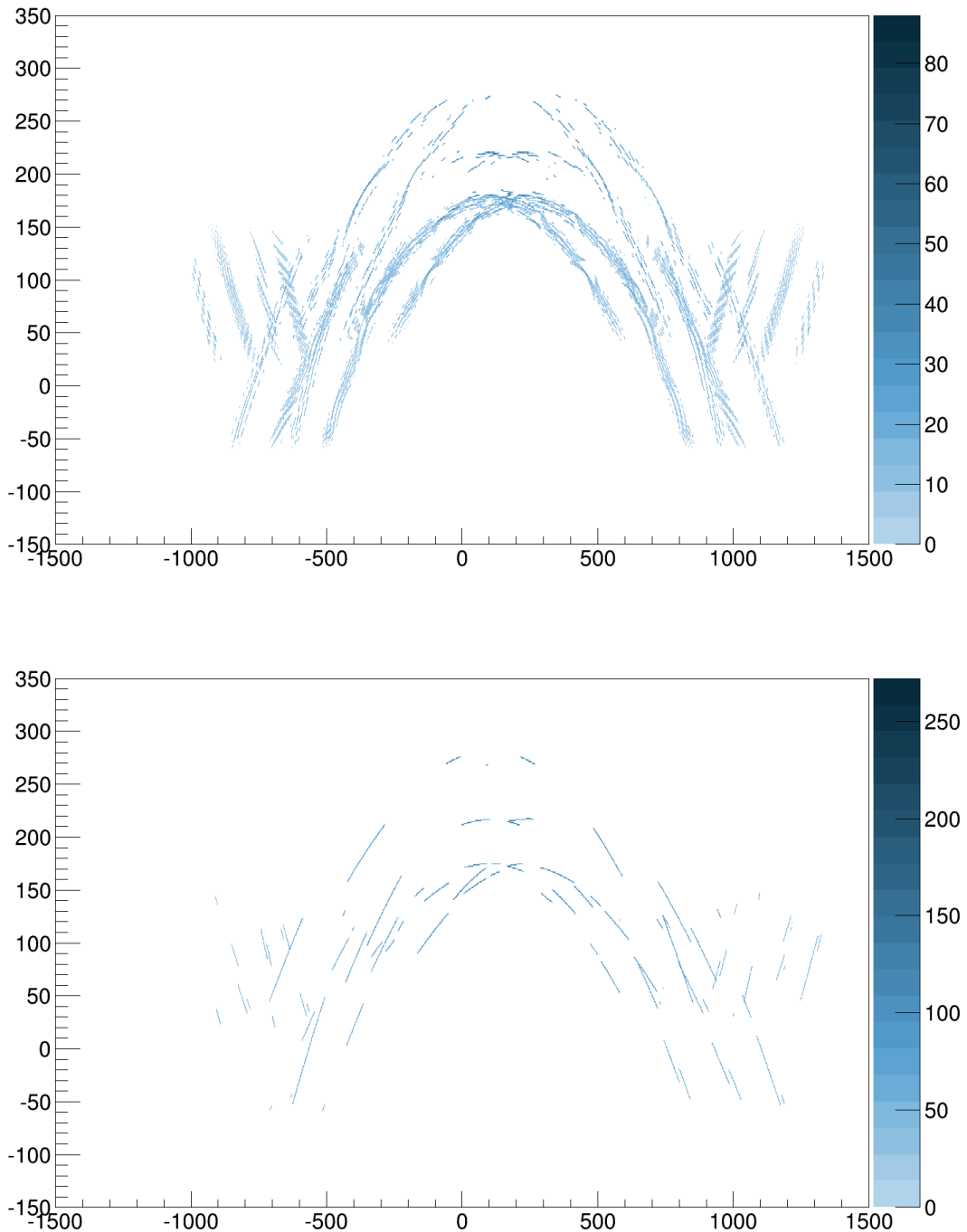


FIG. 12. Images on the PMT plane of the so-called kaleidoscope effect which arises due to the corkscrew paths in the rectangular bars. To make this effect more visible, no pixelization is included and all photons are generated monochromatically to produce these plots. The top plot is for a BaBar DIRC bar, while the bottom plot is for a bar short enough to (almost) remove the effect.

- We do not yet know precisely what the reflectivity of the GLUEX FDIRC mirrors will be. We expect it will be similar to the SLAC FDIRC prototype and so for now we assume that the reflectivities are the same.
- The H12700 PMTs to be used in the GLUEX FDIRC have a much improved quantum efficiency (QE) which will increase the number of photons expected. Using the published active area and QE *vs* λ from Hamamatsu for the H8500 and H12700, we estimate a gain of 15–20% in photon yield.

In total, we expect to have about 10–15% more photons than the SLAC prototype. The photon yield affects the resolution on θ_C as approximately $1/\sqrt{N_\gamma}$; therefore, we expect the uncertainty in the photon yield estimate translates into about a 5% uncertainty on the GLUEX FDIRC resolution on θ_C .

To validate our simulation, we ran it using the SLAC FDIRC prototype as the focusing system. For nearly perpendicular tracks, we obtained a per-photon resolution of about 9 mrad without using timing information in our reconstruction. This is consistent with the value of 9.05 mrad obtained by SLAC in their simulation. Including timing information improves the per-photon resolution by about 5%, which is also consistent with the SLAC results [36].

C. Reconstruction Algorithms

In order to optimize the design, we need to be able to convert the complicated patterns observed on the PMT plane into a Cherenkov angle. The BaBar experiment used a so-called look up table (LUT) approach to determining the θ_C . This method generates a large number of photons at various Cherenkov angles exiting each bar, then tracks them to the PMT plane. For each hit recorded in a PMT pixel, the LUT provides a list of all possible photon propagation vectors that could have led to a photon hitting the pixel. Plotting the cumulative distribution of possible θ_C values for all photons associated to a charged particle provides a means for determining the actual value of θ_C . We have begun work on a similar algorithm using GEANT4 MC to build the table.

An alternative approach is to obtain a probability density function (PDF) for the distribution of photons expected on the PMT plane for each charged-particle hypothesis. Using this PDF and the PMT hits associated to the particle, the likelihood is easily obtained for each hypothesis. Arbitration between particle types is then performed using the likelihood ratio, or equivalently the difference in the log of the likelihoods, formed from two hypotheses. The patterns of photon hits

produced by the FDIRC are complicated and, as of yet, we do not know how to determine them analytically. Instead, we numerically determine the PDFs using Kernel Density Estimation (KDE). The KDE method constructs an estimate for the PDF for a single charged particle as follows:

- a large number (results shown below use $2 \cdot 10^5$) of photons are randomly generated for the particle under a single hypothesis;
- each MC photon is traced to the PMT plane (this is done analytically);
- a three-dimensional (PMT plane location + time of hit) Gaussian function is centered at the hit location and time of each MC photon;
- the (unnormalized) PDF is the sum of these Gaussian functions.

The choice of a Gaussian function is arbitrary, and many other choices can be found in the literature. We tried several options and found minimal dependence on this choice. The procedure is repeated to construct the PDF for alternative PID hypotheses. Since this approach naturally includes timing information, the so-called chromatic effect (λ dependence of θ_C) is accounted for as well as it can be given our timing resolution.

To demonstrate how the likelihood approach works, we consider a charged particle with $p = 5 \text{ GeV}/c$, which is near the edge of the reach of the DIRC for $K - \pi$ separation. Figure 13 shows $\Delta\mathcal{L}_{K\pi}$ for an ensemble of kaons and pions with identical \vec{p} . The corresponding ROC curve is also shown (ROC curves show background rejection *vs* signal efficiency). The resolution on θ_C is extracted by producing the ROC curve for two Gaussian distributions whose means are separated by $\theta_C^K - \theta_C^\pi$ (the nominal Cherenkov angles in quartz for a kaon and pion with this momentum) each with a width σ . The value of σ is varied until the ROC curve matches the one obtained from the KDE-based $\Delta\mathcal{L}_{K\pi}$ method (technically, we find the value of σ that produces the same integral under the ROC curve). The best match from an ideal Gaussian ROC curve is also shown in Fig. 13, which is obtained for $\sigma = 1.74 \text{ mrad}$ for this choice of \vec{p} and optical-system design.

As implemented, this approach takes about $0.1 - 1 \text{ s}$ per particle to run. This algorithm will need to become faster to be part of the GLUEX reconstruction. We are currently working on ways to speed this up and expect to be able to reach an acceptable level of CPU performance. Alternatively, the LUT approach may be used, or some other method not yet considered. The KDE $\Delta\mathcal{L}$ method is used below to study the FDIRC design and performance.

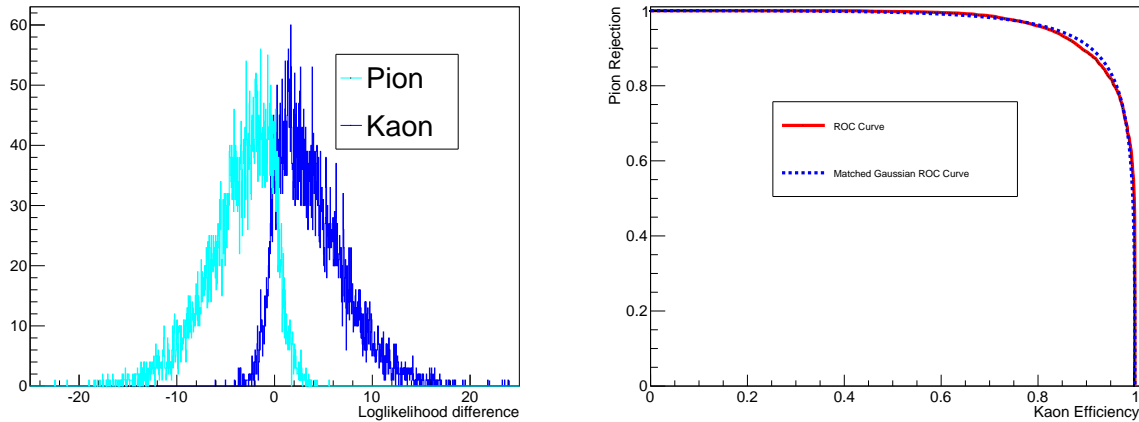


FIG. 13. (left) $\Delta\mathcal{L}_{K\pi} \equiv \log \mathcal{L}_K - \log \mathcal{L}_\pi$ for 4000 kaons and 4000 pions each with $p = 5 \text{ GeV}/c$, $\theta = 4^\circ$ and $\phi = 40^\circ$. (right) Pion rejection *vs* kaon efficiency ROC curve obtained from the same set of kaons and pions.

D. Optimization and Requirements

As our nominal starting point, we choose to copy the optics from the SLAC design for SuperB [36]. In this section, we are only interested in the performance of the PID system; therefore, we do not include the contribution to the resolution on θ_C due to the tracking system. We also do not include multiple scattering of the particle inside the bar at this point since the uncertainty on θ_C due to scattering is momentum dependent and non-Gaussian (also, it is irreducible given that the bar boxes cannot be modified). This complicates quantifying the resolution of different designs. However, the effect of scattering is included in the projected overall performance of the system below. Recall that to achieve the physics goals of GLUEX, the resolution contribution from the PID system alone must be $\lesssim 2.4 \text{ mrad}$.

Since the path length taken by the photons in the focusing box is not constant, the cylindrical mirror focuses some photons but defocuses others. Given that custom cylindrical mirrors are difficult to produce and expensive, we consider whether an alternative (cheaper) approach can produce the same physics performance. Figure 14 shows the hit pattern on the PMT plane obtained using the cylindrical mirror, and using a three-segment approximation of the cylindrical curvature obtained using only flat mirrors (see Fig. 15).

A comparison of the resolution on θ_C obtained from each mirror is shown in Fig. 16. In GLUEX the highest-momentum particles typically have small polar angles, and at these angles the three-segment mirror performs slightly better. However, as can be seen in Fig. 17 for the nominal radius

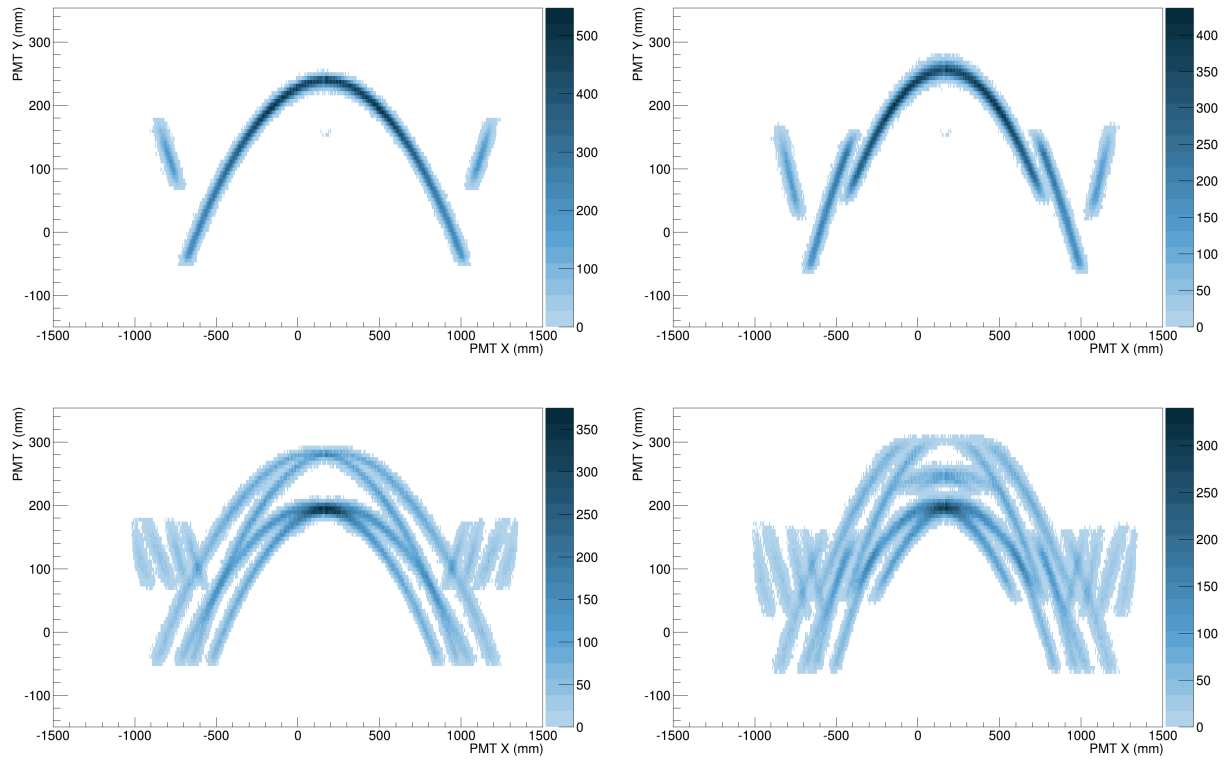


FIG. 14. PMT hit patterns for (left) a cylindrical mirror and (right) three flat mirrors to approximate the cylindrical radius. The top row is for perpendicular tracks, while the bottom row is for $\theta = 4^\circ, \phi = 40^\circ$. These plots are for the nominal cylindrical radius of 1200 mm.

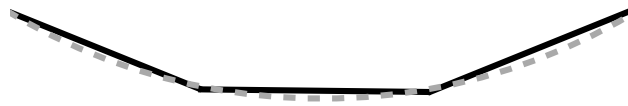


FIG. 15. Schematic comparing the cylindrical and three-segment mirrors.

(we will refer to the three-segment mirror as having a pseudo-radius) the PMT area covered is about 10% larger for the three-segment mirror. Figure 18 shows the resolution on θ_C for different pseudo-radii. It is possible to reduce the radius and, therefore, reduce the PMT area covered with minimal loss in performance. The resolution on θ_C for a fixed PMT area covered is approximately the same for the cylindrical and three-segment mirrors. Therefore, we conclude that the three-segment mirror is the best choice in terms of cost versus benefit. The nominal pseudo-radius of the three-segment mirror is taken to be 800 mm, which is where the PMT area required is the same as

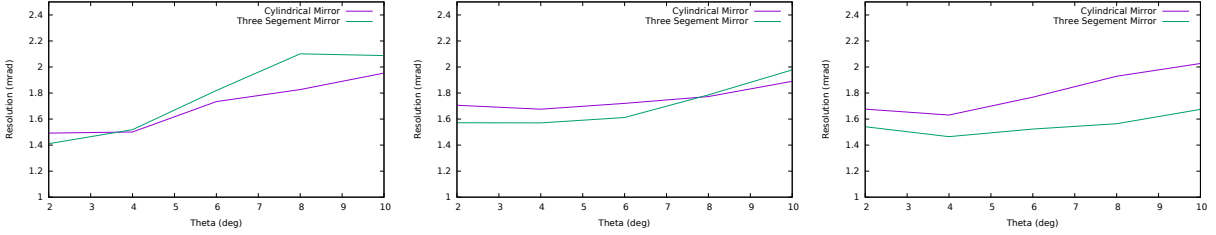


FIG. 16. Cherenkov angle resolution comparing the cylindrical and three-segment mirrors as a function of the charged particle's polar angle θ for (left) $\phi = 0^\circ$, (middle) $\phi = 45^\circ$ and (right) $\phi = 90^\circ$, where θ and ϕ are defined with respect to the normal to the quartz bar.

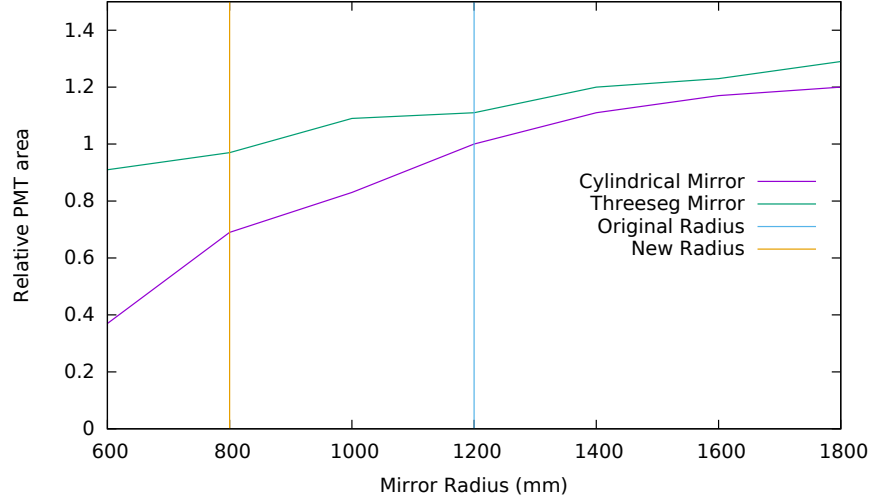


FIG. 17. PMT area required versus mirror radius (or pseudo-radius) relative to the nominal design.

that of the nominal cylindrical mirror from the SuperB design.

The SLAC design optimized the optics for the SuperB experiment. There are several constraints which limit the possibility of improvement for GLUEX:

- Increasing the pseudo-radius of the three-segment mirror improves the resolution but at the cost of more PMTs. Since PMTs are the driving factor in the total cost of the system, increasing the number required is not an option.
- Increasing the path length in the focusing box will also improve the resolution as the pixelation effect will decrease; however, this again is not permissible. Decreasing the path length quickly leads to the pixels dominating the resolution.

We do consider altering the angle of the three-segment mirror relative to the bars, but require the

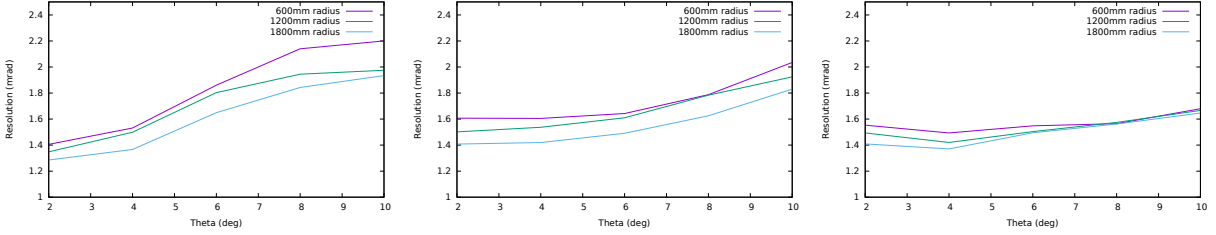


FIG. 18. Cherenkov angle resolution comparing different three segment mirror pseudo-radii as a function of the charged particle's polar angle θ for (left) $\phi = 0^\circ$, (middle) $\phi = 45^\circ$ and (right) $\phi = 90^\circ$, where θ and ϕ are defined with respect to the normal to the quartz bar. The nominal (SuperB) radius is 1200 mm.

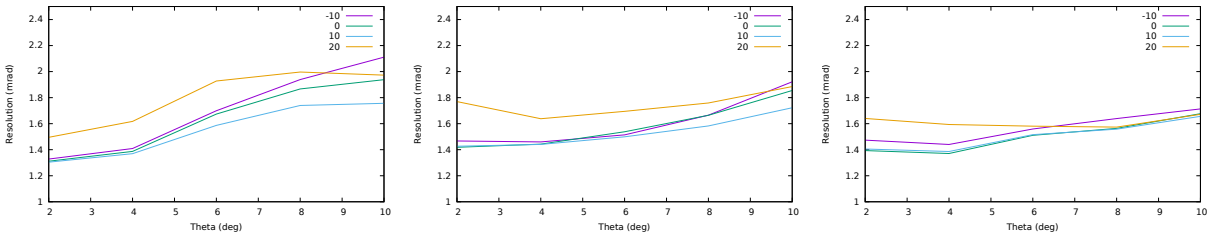


FIG. 19. Cherenkov angle resolution comparing different angles (relative to the nominal design, in units of degrees) of the three-segment mirror relative to the quartz bars as a function of the charged particle's polar angle θ for (left) $\phi = 0^\circ$, (middle) $\phi = 45^\circ$ and (right) $\phi = 90^\circ$, where θ and ϕ are defined with respect to the normal to the quartz bar.

PMT area covered to be fixed. For each angle, the PMT plane is also moved to the optimal location (given its fixed size). Figure 19 shows that the nominal optics are (at least close to) optimal. We are still investigating the optics, but it appears that given the constraints it may not be possible to improve on the SLAC design.

Figure 20 shows the resolution on θ_C versus the distortion of the reflected angle off of the three-segment mirror. The system is most sensitive to image distortions due to this mirror, so we define the performance requirement of the mirror technology using it. The resolution begins to degrade around 1 mrad. This is expected since the uncertainty due to the PMT pixel size is about 3 mrad per photon. We also consider misalignment of the system in our simulation and find that the performance begins to degrade when unaccounted for shifts of $\gtrsim 0.5$ mrad are introduced. This shows that the system must be aligned so that the relative angles between the various components are known to better than about 0.5 mrad. It is important to note that, as shown above, the performance is largely insensitive to what these angles are, but it is sensitive to how well we can determine them after installation. We are currently investigating how best to perform this

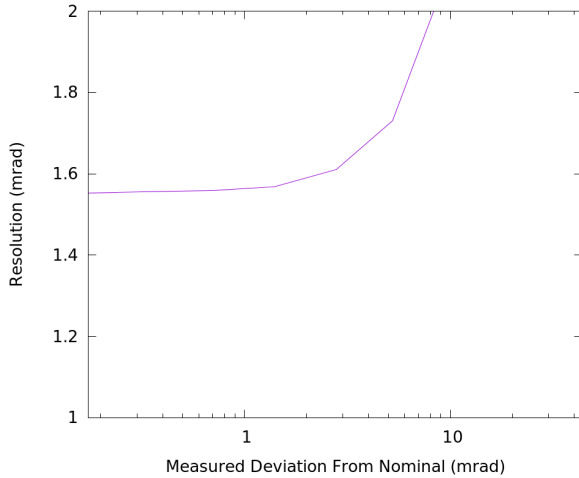


FIG. 20. Resolution on θ_C versus distortion of reflected angle off of the three-segment mirror.

calibration, but certainly using GLUEX data, *e.g.* $K_S \rightarrow \pi\pi$ decays where the displaced vertex and K_S mass identifies the tracks as pions, will play an important role. Preliminary studies using simulated GLUEX events suggest that the physical alignment of the system can be adequately determined *in situ* using such decays.

Figure 21 shows the resolution on θ_C versus the index of refraction of the liquid used to fill the box. The dependence of the performance on n of the liquid is negligible. The performance will, of course, be affected by the transmittance of the liquid. This has led us to choose to fill the box with water (as was used by BaBar). Since the path length is only about 64 cm, the difference of attenuation in distilled compared to deionized water is negligible. We choose to use distilled water to greatly reduce the threat of damage to the mirror and box components. We also note that since all tracks will enter the GLUEX FDIRC at near-perpendicular angles, the angle of incidence of the photons as they exit the quartz and enter the water is very rarely near the critical angle at this interface. Therefore, we expect negligible loss of photons due to reflection.

We now present a breakdown of the various contributions to the resolution on θ_C . Here we only include the uncorrelated errors related to the per-photon resolution; *i.e.*, the effects due to multiple scattering and tracking uncertainties are turned off in the simulation. Without these effects, the FDIRC performance is nearly Gaussian which makes factorizing the remaining contributions straightforward. Table II shows the following contributions:

- The intrinsic resolution of 3 mrad is input to the simulation. This accounts for distortion that occurs during transport along the bars.

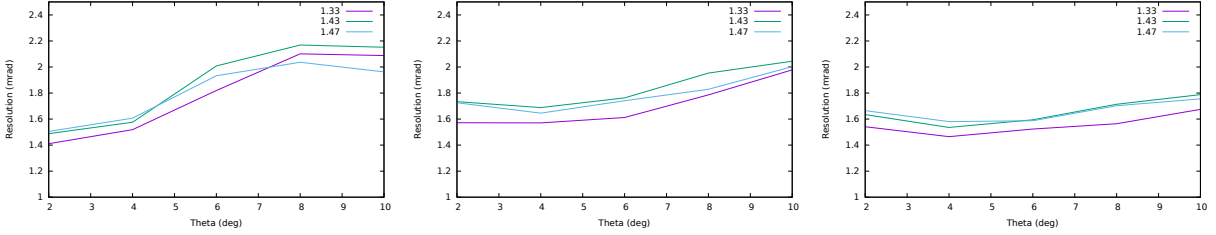


FIG. 21. Cherenkov angle resolution comparing different liquid indices of refraction as a function of the charged particle's polar angle θ for (left) $\phi = 0^\circ$, (middle) $\phi = 45^\circ$ and (right) $\phi = 90^\circ$, where θ and ϕ are defined with respect to the normal to the quartz bar. These results assume the same transmission probability for all n .

TABLE II. Breakdown of uncorrelated contributions to the per-photon θ_C resolution for $\theta = 4^\circ$ averaged over ϕ . Excluding the pixel size, each contribution and the total varies depending on the track trajectory.

Source	Value [mrad]
Intrinsic	3.0
PMT pixel size	2.7
Chromatic	4.3
Kaleidoscope	4.3
Total	7.3

- The PMT pixel size should contribute an uncertainty of approximately pixel width divided by $\sqrt{12}$ divided by the photon path length which gives 2.7 mrad. We estimate this in the simulation by doubling the size of the PMTs, determining the resolution, then extrapolating linearly to zero-size pixels. This approach gives a consistent value of 2.5 mrad.
- The chromatic effect is estimated by comparing the resolution of the system for the default simulation with a simulation where all photons are generated with the same wavelength (mono-chromatic light). The result obtained is consistent with the RMS due to λ dependence of the generated θ_C distribution.
- The kaleidoscope effect is estimated by reducing the length of the bar such that the effect is no longer present.

The various contributions (excluding the PMT pixel size) depend on the track trajectory. Table II gives the values for tracks that enter the bars at a typical GLUEX angle of $\theta = 4^\circ$ averaged over ϕ .

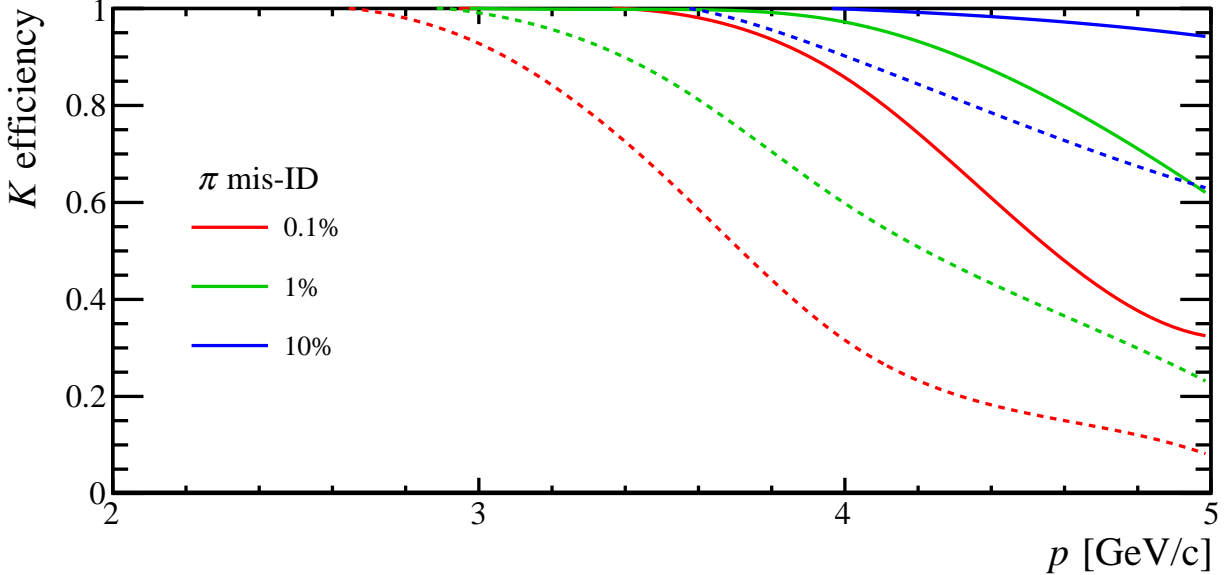


FIG. 22. Kaon efficiency *vs* momentum for pion mis-ID probabilities of 0.1, 1, and 10%. The solid lines show the performance achieved by our current design in simulation, while the dashed lines show the performance assumed in Ref. [3].

Finally, we show in Fig. 22 the expected $K - \pi$ separation obtained by the GLUEX FDIRC. Here we include multiple scattering inside of the bars and the uncertainty due to the GLUEX tracking system. The performance assumed in Ref. [3], which corresponds to a θ_C resolution of 2.5 mrad for all charged particles, is also shown. Our nominal design outperforms the assumptions of Ref. [3].

E. EM Background

Interactions of the photon beam inside the GLUEX detector produce background in the FDIRC from secondary electrons, positrons and photons. This EM background rate is important for two reasons: it will result in noise making determination of Cherenkov angles more difficult, and it will cause more electronic channels to be read out increasing the event data size. The EM background from the beam was simulated using GEANT and the full GLUEX MC. The rate at which particles produced by EM interactions enter the FDIRC is highly position dependent. As can be seen in Fig. 23, the rate falls off exponentially with distance from the beam line. The closest FDIRC bar will be placed 15 cm from the beam. Integrating over the region covered by the FDIRC, we expect roughly 8 photoelectrons per time segment read out by the data acquisition; therefore, the EM background rate will not cause any significant increase in event size. These Cherenkov

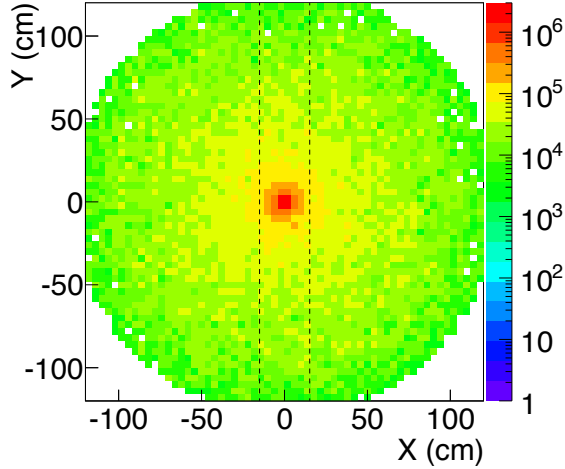


FIG. 23. EM background expected in a plane near the FDIRC (arbitrary normalization). Each bin has a size of $4\text{ cm} \times 4\text{ cm}$. The dashed lines show location of the inner edge of the first FDIRC bar. *N.b.*, this plot was made when we were considering orienting the bars vertically. The current design is recovered by swapping the axes or, equivalently, redrawing the dashed lines horizontally with the same separation.

photons from EM background interactions can be rejected using the measured *vs* expected photon propagation time (as was done in BaBar) and therefore do not impact the particle identification performance of the FDIRC.

F. Effects of the FDIRC on other GlueX Systems

Installing the FDIRC results in a significant increase in material upstream of the FCAL. We have studied the effects of the FDIRC on the FCAL performance using GEANT and found them to be minimal (see Fig. 24). The photon energy detection threshold increases from 160 MeV to 180 MeV. Above 500 MeV the photon reconstruction efficiency is unaffected. The small electron-positron opening angle from converted photons, along with the small distance between the FDIRC and FCAL, results in a single EM shower; therefore, the effect of the FDIRC on photon reconstruction is minimal.

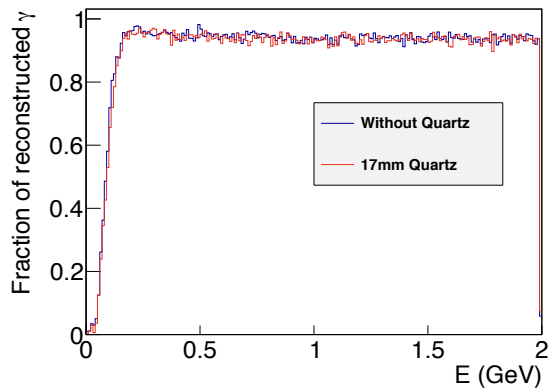


FIG. 24. Effects of the FDIRC material on FCAL photon reconstruction.

IV. FOCUSING BOX DESIGN

A. Mirrors

The requirements of the mirrors are: they must be highly reflective in the 300–600 nm range; the distortion of the reflected angle must be $\lesssim \mathcal{O}(1 \text{ mrad})$; and they must be resistant to distilled water (see Sec. III). Custom optical-quality mirrors can satisfy these requirements; however, covering the large surface area required with such mirrors is prohibitively expensive. Instead, we are currently investigating two alternative options:

- First-surface glass mirrors attached using 3M VHB tape to an aluminum strongback. The mirror substrate is float glass that is coated on the front surface with aluminum and an interface coating to enhance reflectivity. Producing these mirrors requires machining the aluminum strongback (no special equipment needed), followed by taping the glass mirrors to the aluminum (which we can do ourselves). We have purchased a small test mirror produced for hiding a TV embedded in a wall. We are also in contact with both the glass manufacturer and the coating company, and are exploring possible custom coatings, *etc.* Details provided in Table III below. See Fig. 27 for a photo of the aluminum backing for the large flat mirror, and Fig. 25 for photos of attaching the glass to the aluminum.
- Aluminum mirrors with a proprietary coating that provides UV reflectivity and protection from the water. Producing these mirrors requires machining the aluminum, depositing nickel on the surface, lapping and polishing the surface prior to applying the coating. Each step must be performed by a vendor (see Table IV for details). See Fig. 26 for prototype samples at various stages of the process.

The first-surface glass mirror option is less than half the cost of the polished-aluminum option, but even the polished-aluminum option is less than half the cost of using custom optical-quality mirrors. The first-surface glass mirror option is incredibly cost-effective, requires no special machining equipment, and uses readily available commercial products. Therefore, if these mirrors meet our needs, we will use them. Below we present some initial studies of the first-surface glass and aluminum mirrors.

To characterize the mirrors, we have set up an optical bench at MIT/Bates Lab. A CMOS camera (see Table V) is placed near the center of a spherical mirror (see Table VI). An unpolished fiber that carries various wavelengths of light is placed directly opposite from the camera (near

TABLE III. Specs for the first-surface glass mirrors on aluminum strongback.

	Details
Aluminum base	Machine, heat treat, finish; flatness tolerance 12.5-25 μm
VHB tape	made by 3M
First-surface glass mirror	Microcorrugation $\leq 20\mu\text{m}/20\text{mm}$; Al+ interface coating

TABLE IV. Specs for the aluminum mirrors.

	Details
Aluminum base	Machine, heat treat, finish; flatness tolerance 12.5-25 μm
Nickel coat	0.006–0.009 in thick; medium phosphorus
Lap surface	flat to 0.001 in
Polish surface	special equipment required
Reflective coat	ECI #801SP UV-Al

the center of the spherical mirror) so that the image of the fiber is focused onto the CMOS plane. Light of different wavelengths is obtained from several LEDs. Figure 28 shows a schematic for this control setup. Normalizing to the amount of light collected during a fixed time interval with each LED in this setup avoids the need for explicit knowledge of the reflectivity of the spherical mirror, luminosity of the source, and efficiency of the camera.

To measure the reflectivity and angular distortion, the flat mirrors are placed into the setup at two angles (14 and 45°) as shown in Fig. 29. The angles expected in the FDIRC are $\gtrsim 45^\circ$; however, reflectivity is typically measured at smaller angles. To permit comparison to reflectivity values provided by vendors, we make the additional measurements at small angles. The reflectivity

TABLE V. Specs for the camera used in the mirror characterization.

Model	DCC1545M
Sensor	CMOS
Color	Monochrome
Resolution	1280 x 1024 pixels
Sensor Dimensions	6.66mm x 5.32mm
Dynamic Range	68.2dB
ADC Resolution	10 bit

TABLE VI. Specs for the spherical mirror used in the mirror characterization.

Diameter	75mm
Clear Aperture	> 90% of diameter
Surface Irregularity	$\lambda /4$ at 633nm
Surface Quality	40-20 Scratch-Dig
Diameter Tolerance	+0.0 mm/ - 0.2 mm
Substrate	N-BK7

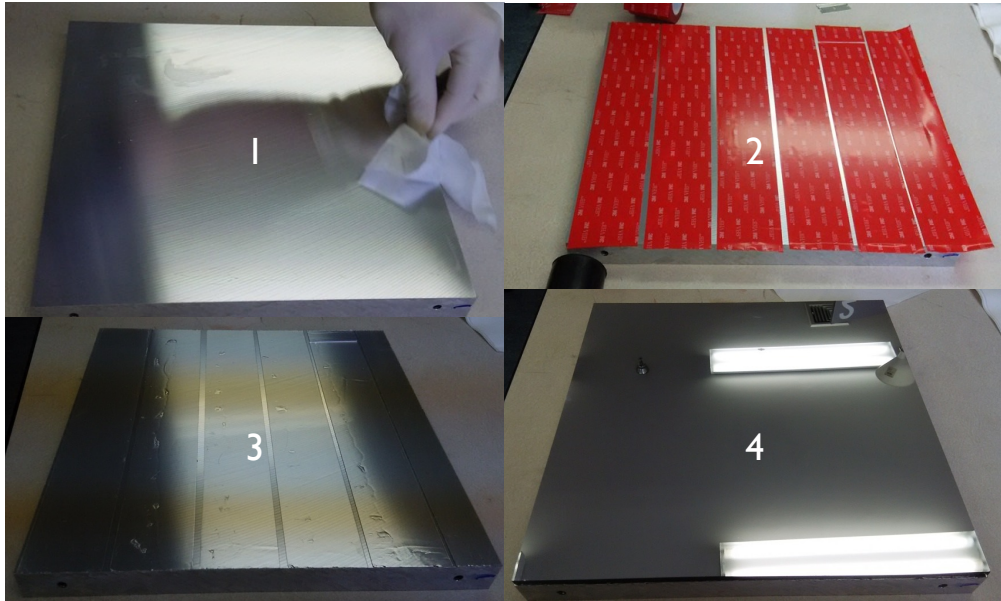


FIG. 25. Steps for attaching the first-surface glass mirrors to the aluminum strongback applied to a small test piece at MIT/Bates.

measurement involves collecting the total amount of light in the image during a fixed time interval in both the control setup of Fig. 28 and in the setup of Fig. 29. The light in the latter setup makes two bounces off of the flat mirror and one off of the spherical mirror. Taking the ratio of the light collected in the two setups cancels the reflectivity of the spherical mirror, along with the light output of the source and the efficiency of the camera. Therefore, the reflectivity of the flat mirror is obtained as the square root of the ratio of light measured in these two setups. We note that the amount of light collected is linearly proportional to exposure time.

The 45° setup not only provides the same approximate bounce angle as in the FDIRC, but we also configured it to have the same mean photon path length. Figure 30 shows some example



FIG. 26. Aluminum mirrors after (left) machining, (middle) lapping, and (right) lapping and polishing. Each sample has been coated with nickel, but not yet been coated with the ECI UV-Al reflective coating.

images obtained using a blue LED at 45° for the aluminum and glass mirrors. The size of one PMT pixel is also shown to aid in judging the image distortion. The quality of the aluminum mirrors is such that scratches on the surface of the fiber (which is 1 mm in diameter) are resolved. The image distortion due to the aluminum mirrors is too small to measure, but clearly the number of photons reflected into another pixel would be negligible. The image distortion due to the glass mirror is visible but still negligible compared to the size of the PMT pixel. We estimate the distortion to be $\lesssim 0.2$ mrad, which is well within our tolerance. (The less than symbol is used because it is difficult to focus the image. We think that some of the fuzziness is due to lack of focusing in our setup, rather than distortion due to the mirror. The measurements are being repeated to check this.)

The aluminum mirrors are currently at ECI being coated, so here we only measure the reflectivity of the glass. Figure 31 shows some example light intensity distributions measured in the 45° setup. To obtain the background shape, we take data with the spherical mirror covered. This approach accounts for background light that comes from the source. The background is normalized to match the data away from the signal peak, since the background varies in scale at $\mathcal{O}(1\%)$ in different runs due to light leakage into the room from outside. The background shape, including some hot pixels, describes the data away from the peak well enough for this study. We only count as signal the excess over the expected background within 120 pixels of the maximum intensity, which corresponds to a signal width of 1.25 mm (recall that the image has a width of 1 mm using mirrors with no distortion) and discards minimal signal light. The efficiency of the camera to UV light is lower and, therefore,

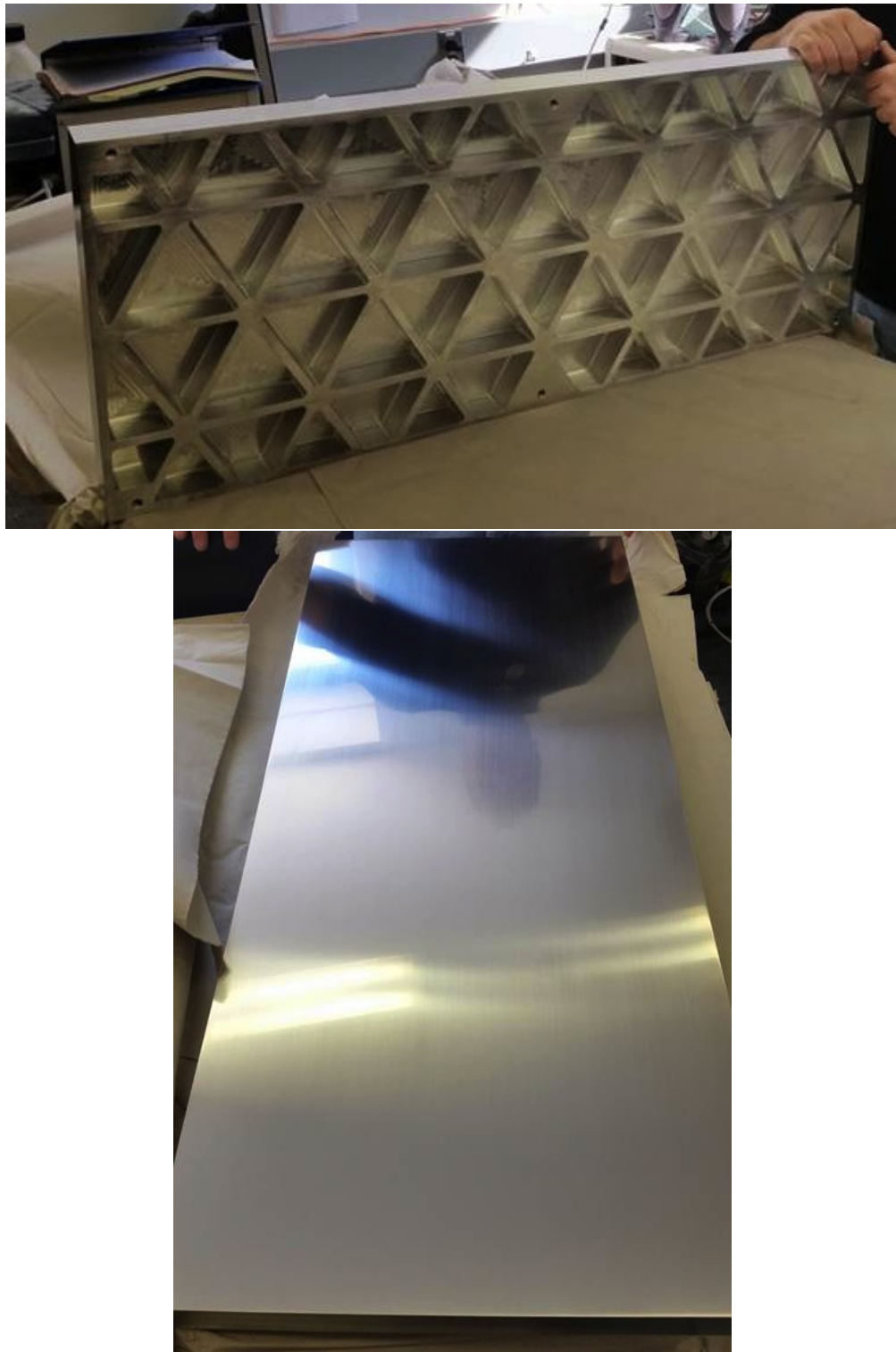


FIG. 27. Large flat mirror (1.1 m long) machined aluminum backing prototype.

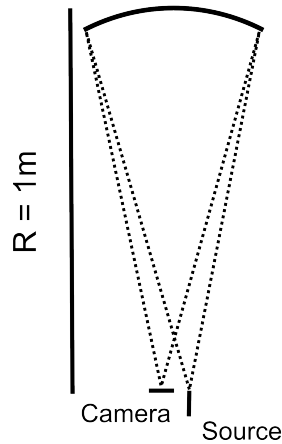


FIG. 28. Setup for the control images. Provides the base measurement for the reflectivity measurements.

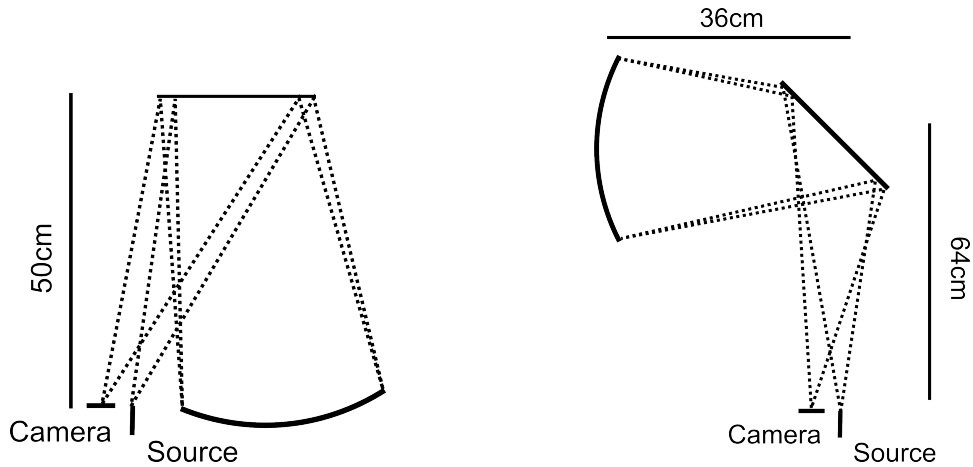


FIG. 29. Setup for reflectivity and angular distortion measurements at reflection angles of (left) 14° and (right) 45° .

we need to collect data for a longer duration when measuring the reflectivity at UV wavelengths resulting in higher background levels. We are in the process of acquiring a visible-light filter to mitigate this.

Figure 32 shows the results obtained for the glass mirror at 14° and 45° degrees for various wavelengths. The measured reflectivity at 14° agrees well with the expected performance reported by the company for an unspecified small angle. The reflectivity measured at 45° is 90–96% in the wavelength region 320–470 nm. The producer of the glass mirrors does not provide data at

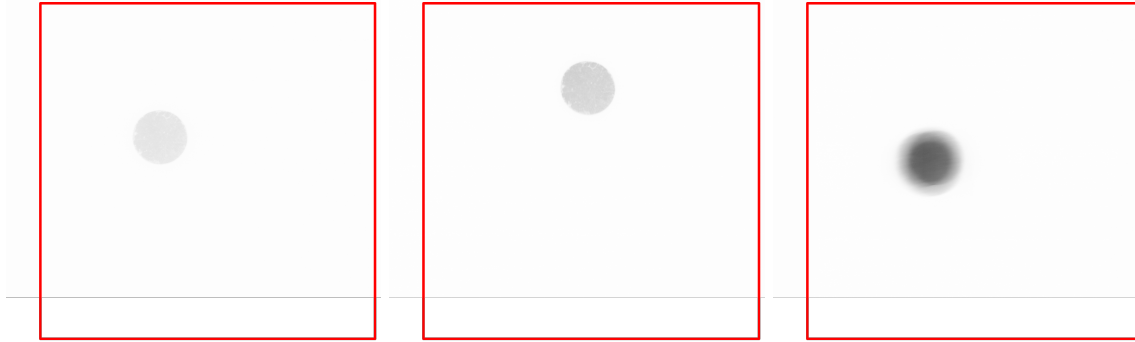


FIG. 30. Example images obtained from the 45° setup in Fig. 29 using the aluminum mirror (left) lapped only and (middle) lapped and polished. The right image is for the glass mirror. The red box shows the size of one PMT pixel (arbitrarily located). No distortion of the image is detectable using the aluminum mirrors as even the scratches on the surface of the optical fiber are resolved.

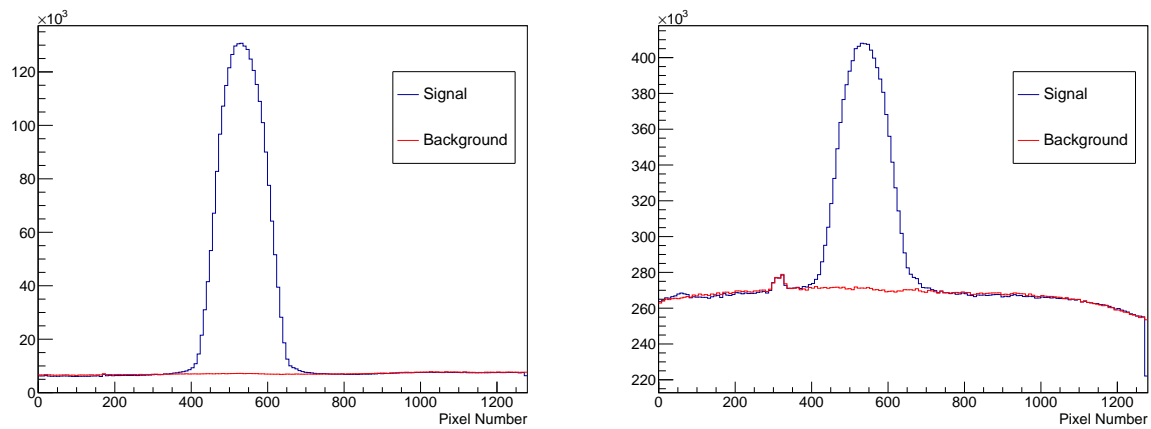


FIG. 31. Example intensity distributions used to measure the reflectivity. Shown are for the glass mirror aligned at 45° using (left) blue and (right) 345 nm LEDs. The background shape is obtained by taking data with the spherical mirror covered.

larger angles; however, the difference we measure in the reflectivity at small and large angles agrees with the difference provided by the maker of the UV-enhanced coating on our spherical mirror (ThorLabs). If these results are accurate, then the glass mirror reflectivity meets our requirements over the full wavelength region of interest. However, since the efficiency of our camera decreases with wavelength, if the LEDs have some visible component then our measurement may be skewed. Adding a visible-light filter in front of the camera will determine if this is the case. Finally, we note

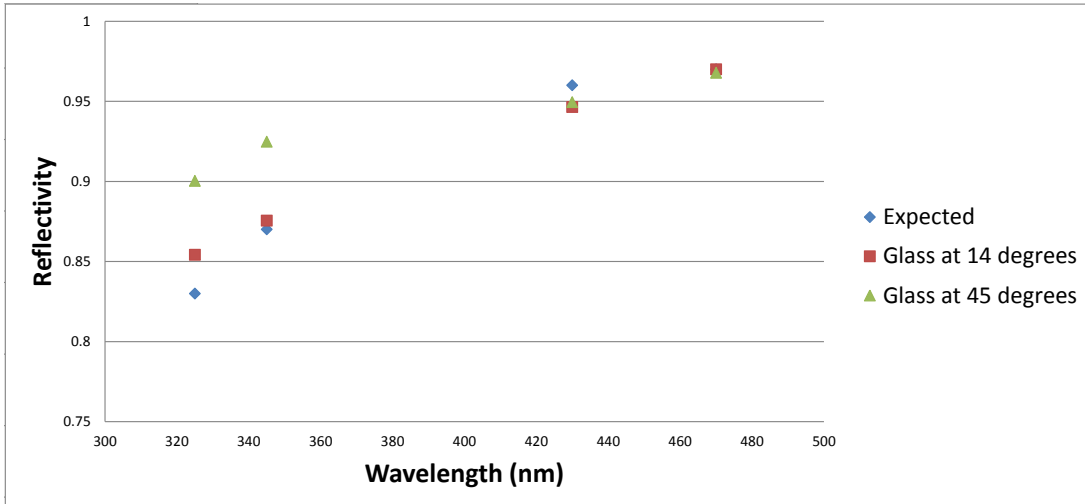


FIG. 32. Reflectivity of the glass backed mirror at 14 and 45 degrees as compared to expected value. *N.b.*, the expected value reported by the company is for a small angle; we do not know the precise value.

that the reflectivity of the mirrors may decrease when submerged in water. Based on information provided by vendors, we expect this to be a few percent effect. We are looking into ways to study this ourselves.

A test glass-taped-to-aluminum mirror has been submerged in distilled water at MIT/Bates Lab since the first week of August. Thus far neither the tape nor the glass mirror show any negative effects due to interaction with the water. After 7 weeks submerged, we redid the reflectivity tests and obtained consistent results as prior to placing the mirror in distilled water. We will continue to monitor this sample, including making periodic reflectivity measurements. The aluminum mirrors are currently being coated (the final step). We should be able to test their reflectivity by early October. In summary, both mirror technologies considered provide affordable options, and both

can be produced relatively quickly. Tests are ongoing but it appears that both methods are viable. Furthermore, we are exploring custom coatings and other possible improvements to the mirror design. Unless a problem arises, the first-surface glass mirrors will be selected due to their low cost and ease of production.

B. Box Design

Figure 9 shows a schematic diagram of the focusing box. We are still finalizing some of the details, but the most important aspects of the design are:

- The box will be made of stainless steel, welded, but have at least two removable plates. It will also have a removable quartz window for the PMTs.
- The PMTs will be mounted such that they are in optical contact with the window, but not with the water. The PMTs will be serviceable *in situ*; *i.e.* they will be removable without draining the tank or causing misalignment.
- The box will be filled with distilled water. The water will be continuously circulated through an external system that will maintain correct pH (to prevent damage to the metal components) and remove gases and biologicals.
- The mirrors will be mounted quasi-kinematically using three mounting points each to a separate sub-frame. Each will employ flexures to minimize deformation of the mirror itself. The sub-frame will permit mounting and adjusting the mirrors as a unit prior to installation inside the focusing box.
- A hermetic seal between the focusing box and the bar boxes will make use of the existing elastomer sealing interface on the bar boxes. The bar boxes will be supported independent of the focusing box. Negligible force will be transmitted through the boot.
- The bar boxes will be aligned relative to the focusing box before mating the two. The external frame that supports both the bar boxes and focusing box is to allow controlled, precise motion such that the bar boxes can be inserted into the focusing box once aligned.
- The focusing box will be mounted vertically in Hall-D.

The H12700 MaPMTs need to be coupled to the quartz window of the focusing box. An optical grease may be used to reduce the photon loss in the air gap between the window and MaPMTs. Eljen EJ-550 [49] is an optical grease with good optical transmission for wavelengths greater than 300 nm, which has been used successfully in prototypes of the PANDA DIRC.

Our current baseline design uses two separate ~ 1 m long focusing boxes that will each provide readout for two of the BaBar boxes. As discussed earlier, this introduces one side reflection for most rings, relative to the design option with a single box that is just over 2 m in length. Our simulation shows that the folding due to this reflection has negligible impact on the θ_C resolution. Figure 33 shows a schematic diagram for a ≈ 1 m box. Work is ongoing to develop a full prototyping/construction plan for the focusing box (see Sec. VIII). We also need to decide how to interface the water-circulation system with the box(es). That being said, we do not expect to encounter any major obstacles with the box itself.

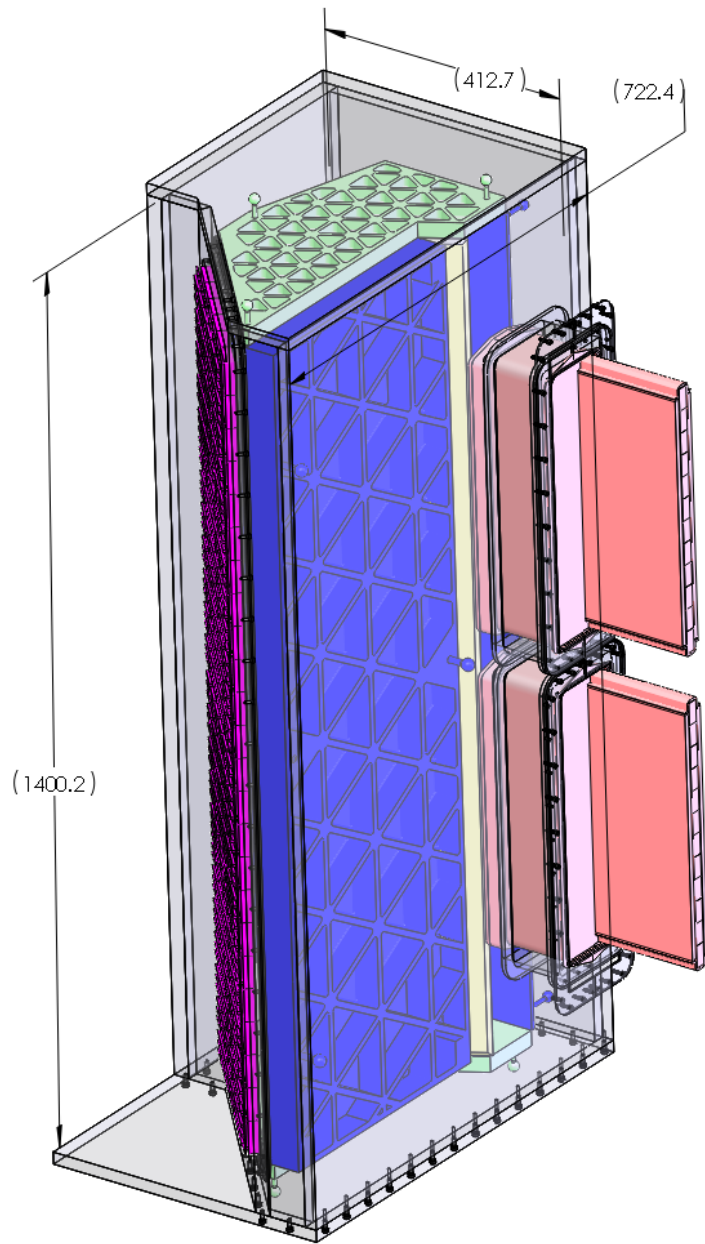


FIG. 33. Schematic diagram of the focusing box with details on mirror mounts, *etc.* The length of the box has not yet been finalized.

V. PHOTON DETECTION AND READOUT

A. Introduction and Requirements

The imaging of Cherenkov photons for the GLUEX FDIRC detector requires a two-dimensional photodetector with good position resolution. The yield of produced Cherenkov photons is proportional to $1/\lambda^2$; however, due to the materials used in the BaBar quartz bars (especially the EPOTEK 301-2 glue [31]) only photons with wavelengths longer than 300 nm exit the bars and enter the focusing box. Therefore, the photodetectors are only required to cover the wavelength range above 300 nm. In addition, the readout needs to tolerate the fringe magnetic field from the GLUEX solenoid which is about ~ 25 Gauss. Given these requirements, we considered multi-anode photomultipliers (MaPMT) from Hamamatsu, Micro-channel plate (MCP) PMTs from PHOTONIS and the newly developed large area picosecond photodetectors (LAPPD) using micro-channel plate (MCP) technology [37]. The LAPPD detectors are an innovative solution providing superior time resolution, but they are not currently available in the size and quantity that we require. The MCP-PMTs from PHOTONIS also provide excellent time resolution and tolerate high magnetic fields, however these features are not critical to our design. Therefore, we have selected the MaPMT photodetector option for the GLUEX DIRC, which meets the required performance parameters, have lower unit cost and are readily available.

The expected trigger rate for the highest intensity portion of the GLUEX run plan is about 200 kHz with an expected trigger latency of $\sim 3\mu s$. The readout electronics are required to sustain such a rate with minimal dead time and accommodate the latency of the trigger. The front end electronics must be sensitive to single photoelectrons produced by the Cherenkov photons which have propagated through the optical system. The electronics must compensate for the spread of possible gains for the individual anodes within a given MaPMT within factors of 2–4. Finally, the crosstalk between electronic channels should be smaller than the MaPMT anode cross talk, typically at the level of a few percent.

The readout requirements for the GLUEX FDIRC and CLAS 12 RICH detectors are similar. To minimize duplication of effort and to reduce technical risk, we have chosen to model our readout design after the one developed for the CLAS12 RICH. The CLAS12 collaboration and the JLab fast electronics group have done extensive development work on this system, and proven that it meets the required specifications. A summary of the design is described in the following sections, which borrow heavily from the CLAS12 RICH Technical Design Report [52].

B. Multi-Anode Photomultipliers

Multi-anode photomultipliers have recently been extensively evaluated for various Cherenkov detectors, including the focusing DIRC detector for SuperB [38], the RICH detector for CLAS12 [40, 41], the light gas Cherenkov counter for SoLiD [39], and the RICH detectors for LHCb [42]. Studies initially focused on the H8500 MaPMT assembly [43] manufactured by Hamamatsu Corp. Recently, Hamamatsu introduced the H12700 MaPMT assembly (seen in Fig. 34) [45] with the same geometry and output pin layout as the H8500. The newly optimized dynode structure and voltage scheme of the H12700 provides better separation of single photon signals from background, as shown in Figure 35. In addition, Fig. 36 shows a comparison of the cathode sensitivity and quantum efficiency of the H8500 [43] and H12700 [45] from Hamamatsu, where the quantum efficiency is enhanced for the H12700. The CLAS12 RICH collaboration has also performed comparative studies between the H8500 and H12700 and found that the H12700 has significantly improved performance for single photon detection due mainly to an improved quantum efficiency. Therefore, we select the H12700 for the GLUEX DIRC readout.



FIG. 34. The H12700 multi-anode photomultiplier manufactured by Hamamatsu.

The H12700 [45] flat panel MaPMT assembly has an active area of $48.5 \times 48.5 \text{ mm}^2$. It has an 8×8 anode readout array, and each anode covers an area of $6 \times 6 \text{ mm}^2$. The packing factor of H12700 is a very tight 87% and this makes it very suitable for large area photon detection. The area of the readout plane of the focusing box in the nominal design is about 0.6 m^2 , which requires 216 MaPMTs and correspondingly ~ 14000 independent anodes and readout channels. The H12700 is sensitive to photons with wavelengths between 300-600 nm, which is well matched to the GLUEX FDIRC requirements. In addition, with a time resolution less than 1 ns (Transit Time Spread is around 0.3 ns), the H12700 provides useful time information for disentangling Cherenkov photons

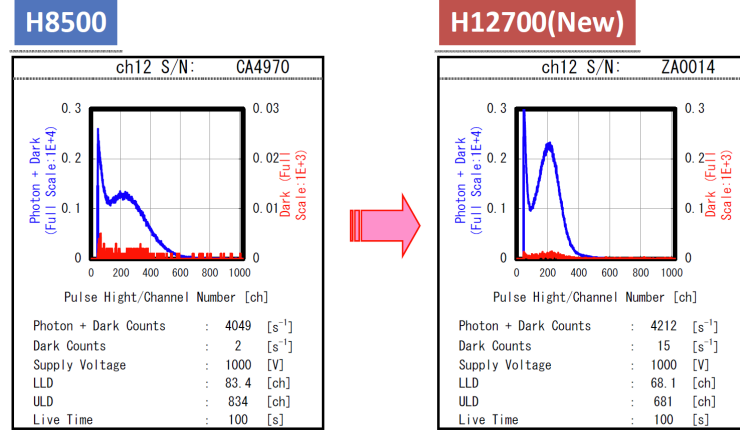


FIG. 35. Improvement of H12700's single photon detection capability [46].

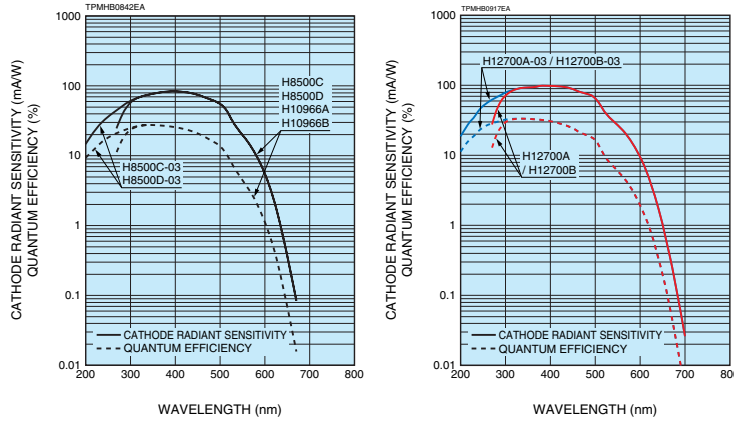


FIG. 36. Comparison of cathode sensitivity and quantum efficiency for H8500 [43] and H12700 [45].

that came directly from the charged particle interaction to the focusing box, and those that traveled to the other end of the quartz bar where they were reflected by the mirror.

The performance of the H12700 in the presence of an external magnetic field was studied in the context of the LHCb RICH upgrade [42]. This study showed that magnetic fields at the level of ~ 25 Gauss can reduce the single photon detection efficiency by $\sim 25\%$ for pixels on the peripheral area of the MaPMT, but pixels in the central area are relatively unaffected. Magnetic fields of this magnitude will be present in the region where the MaPMTs will be located in GLUEX. Passive magnetic shielding will be required to reduce the field to tolerable levels. In Ref. [42] the field was shielded locally with a thin layer of Skudotech [47] (similar to MUMETAL) around each MaPMT, which successfully restored the single-photon efficiency for magnetic fields up to ~ 25 Gauss. This local shielding is a possibility for GLUEX, but would introduce an air gap in the interface between

the MaPMTs and the fused silica window of the focusing box. Therefore, we plan to utilize a large iron shielding box, which will encapsulate the focusing box and shield the region near the MaPMTs. As this region is not in the active area of the detector, there are no requirements on the material budget for the steel shielding box.

The dark rate for the H12700 was also studied in Ref. [42], where the rate of events which are above the single photo-electron threshold was very low (≤ 15 Hz per pixel) for most of the pixels. Therefore, dark currents should be a negligible source of noise for the FDIRC.

An additional source of noise for the BaBar DIRC was caused by low energy photons and neutrons from beam interactions at the PEP-II accelerator [30]. These photons and neutrons interacted with the large water volume, generating additional electrons and positrons which emit Cherenkov light causing addition noise in the readout. This was an important consideration in SLAC's focusing DIRC design for SuperB to reduce the size of the expansion volume, and as mentioned earlier, the volume of water in the GLUEX focusing box is 25 times smaller than the original BaBar DIRC, making it less susceptible to this type of background. The neutron flux in Hall D has been simulated to study the effects of radiation damage to silicon photomultipliers [48]. The simulated 1 MeV equivalent neutron fluence in the region of the barrel calorimeter's silicon photomultipliers is $20\text{-}30 n_{eq}/s/cm^2$. An initial measurement of the radiation dose in the region of the focusing box was made during beam commissioning in Fall 2014 where an integrated does of less than one mrem was delivered over a week. To better understand our sensitivity to these backgrounds we plan to measure the neutron dose with a dedicated probe in the region of the DIRC focusing boxes in Hall D during the next expected beamtime in Fall 2015 or Spring 2016. We will evaluate the results of these measurements and consider possible further tests as necessary.

C. Electronics

The electronics design for the GLUEX FDIRC closely follows the design for the RICH detector for CLAS12 [51], due to the similar requirements for the two detectors and to minimize technical risk. The core of the design is the MAROC3 chip [53] which is specifically designed for the readout of 64-channel MaPMTs. As shown in the diagram of the readout scheme in Figure 37, the MAROC3 chips digitize the analog signals from the MaPMTs and pass the resulting binary data stream to a digital FPGA board. The FPGA not only processes the data on board, but also controls and provides triggers to the MAROC3 chips. The processed data from the FPGA will then be transmitted to

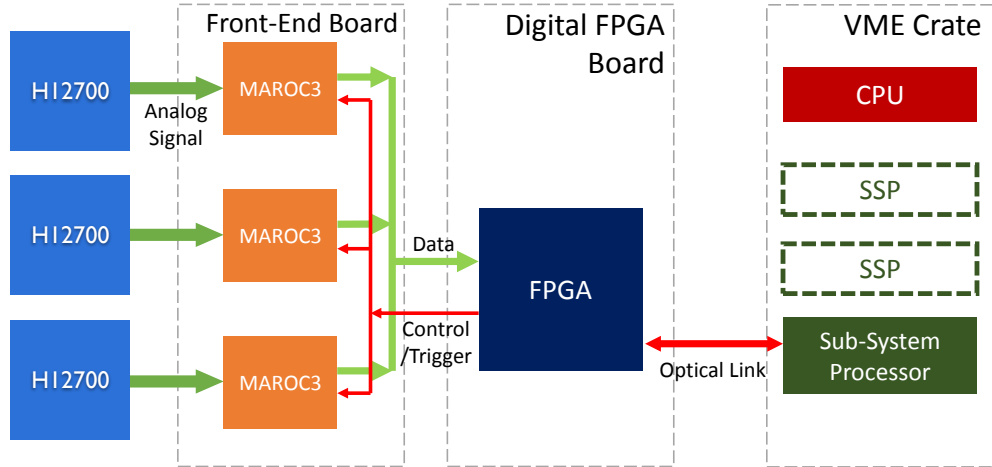


FIG. 37. Readout scheme of the CLAS12 RICH and GLUEX FDIRC.

a Jefferson Lab developed Sub-System Processor (SSP) [54] hosted in a VME crate through high speed optical links, which seamlessly integrates into the current Hall D DAQ system. The front end (ASIC) board has already been developed by the INFN group, and the digital FPGA board has already been developed by the Jefferson Lab fast electronics group. Pictures of preliminary boards are shown in Fig. 38 and 39. These two groups together have demonstrated the feasibility of using the MAROC3 chips for the CLAS12 RICH readout in recent project reviews.

Two of the requirements for the readout electronics are more restrictive for the GLUEX FDIRC than for the CLAS12 RICH and are described further here, while the remaining requirements have already been addressed in the CLAS12 RICH Technical Design Report [51]. The maximum GLUEX trigger rate is about 200 kHz, which is roughly ten times larger than the CLAS12 rate. The most substantial effect this may have on the design is the readout rate which the system is capable of, which could impact the live time of the DAQ system.

The time required to read out a single module of three MaPMTs from the MAROC chips to the SSP is determined by the 2.5 Gbps serial link between the FPGA board and SSP. For a given module, the data rate can be computed with the following equation:

$$\text{Readout time} = [(19 \text{ bits} \times 64 \text{ channels} + 17 \text{ bits} \times 8 \text{ sums}) \times \text{occupancy} + 12 \text{ bits}] \times 3 \text{ MAROC}/2\text{Gbps}$$

where the 19 bits provide the binary hit time for individual pixels, the 17 bits provide times for the MAROC sum lines, and the 12 bits is the ADC of a single pixel for monitoring. Using simulated γp collisions events from PYTHIA with a GEANT model of the GLUEX FDIRC, the maximum occupancy for a single pixel is determined to be 0.7%. Therefore, the expected readout time is

~ 32 ns which at a 200 kHz trigger rate leads to a dead time of less than $\sim 1\%$.

The contribution from the FDIRC to the total event size has been studied with the JLab fast electronics group [50], in relation to the DAQ live time. Each hit pixel constitutes a 32-bit word containing its time and location. Based on this hit size and some overhead for event headers, the DAQ live time is shown as a function of the trigger rate in Fig. 40 assuming a 1 Gb ethernet output for the SSP. Using the same PYTHIA simulations as described above, the occupancy over the entire detector is only 0.35%, which contributes zero dead time for the required 200 kHz trigger rate.

A complete block diagram for the components of the readout system is shown in Fig. 41. Adequate space for these components is already available in the crates installed on the FCAL platform in Hall D.



FIG. 38. ASIC board produced for the RICH detector for CLAS12 with MAROC chips installed [55].



FIG. 39. FPGA board produced for the RICH detector for CLAS12 with ASIC board attached [55].

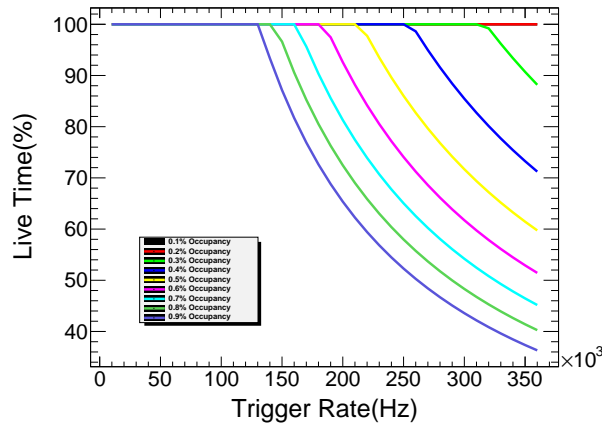


FIG. 40. DAQ live time as a function of trigger rate for occupancies ranging from 0.1% to 1.0% [50]

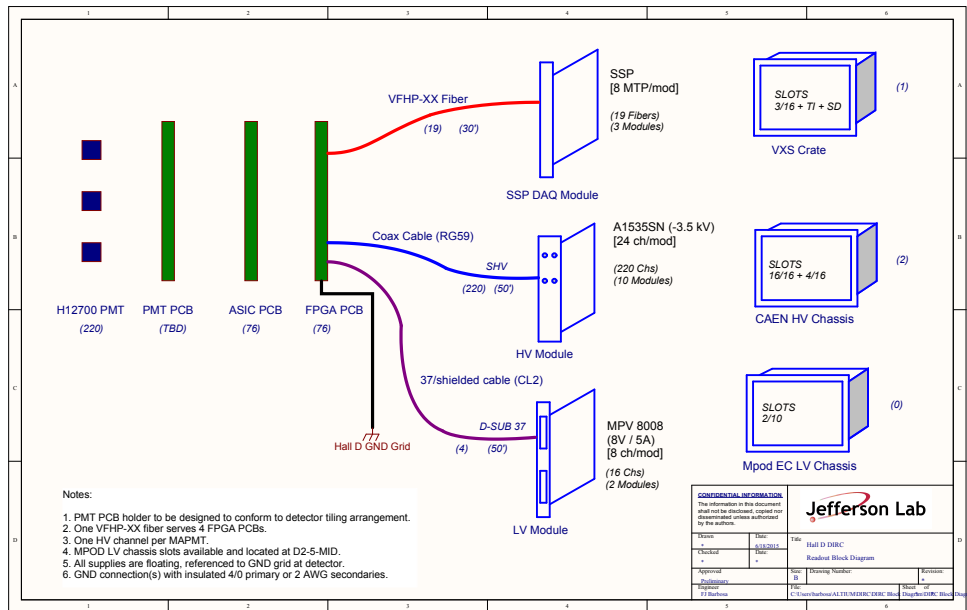


FIG. 41. Block diagram for the DIRC readout components and the required electronics modules and crates, as well as high and low voltage systems.

VI. MECHANICAL DESIGN, INTEGRATION AND INSTALLATION

As noted earlier, the existing GLUEX design has space reserved for a particle identification device between the downstream end of the solenoid and the forward carriage that supports the time-of-flight and the forward calorimeter. The boxes were originally designed for horizontal orientation during the BaBar Experiment. The BaBar detector held the bar boxes in a series of tracks, in which corresponding bearings on the bar boxes roll. The original BaBar detector held the bar boxes in a radial arrangement, around a Central Support Tube. The rails supporting the bar boxes were affixed in the detector by lightweight aluminum bulkheads, themselves supported by aluminum I-beams. Thin aluminum sheet covered both sides of the support tube, further adding strength. The proposed concept design for the GlueX support structure shares many of these features. Much of the Central Support Tube was assembled using a durable two part epoxy, in lieu of mechanical fasteners. This included the joint between the bar box rails and the aluminum bulkheads. To ensure proper alignment of the bar box rail sections, the rail components were held within the bulkheads by fixtures and epoxied in place. It is proposed that similar assembly procedures used for the Central Support Tube eventually be used on the GlueX horizontal support structure.

The proposed GlueX support structure, shown in Fig. 42, consists of two bulkhead frameworks, stacked one atop another. The frames are centered vertically and horizontally on the beam line. I-beams form the outer perimeter of each bulkhead framework; the two beams closest to the beam line will be constructed with a low-density high-strength material like carbon fiber. Each of the frameworks is structurally independent of one another, and will be constructed separately. The frameworks attach to a pair of vertical guide rails on the support structure using linear bearings. A pair of lead screws with mechanical drive can be used to move the each framework vertically. This arrangement allows the detector to be conveniently moved away from the active area of the forward calorimeter in anticipation of experiments that may want to reduce material in front of the calorimeter.

To compensate for inherent misalignment in the beams, bar box rails, *etc.* it is proposed that the connection between the I-beams and the bulkheads incorporate a T-slot, as shown in Figure 43. When the bar box rails are attached to the bulkheads a fixture will maintain the distance between the rails (gauge), thus sufficient accuracy and precision should be fairly attainable in that respect. However any lateral bowing in the I-beams or tracks would be more difficult to eliminate pre-assembly. T-slots would allow the bulkheads to be adjusted to eliminate binding in the rail-bar

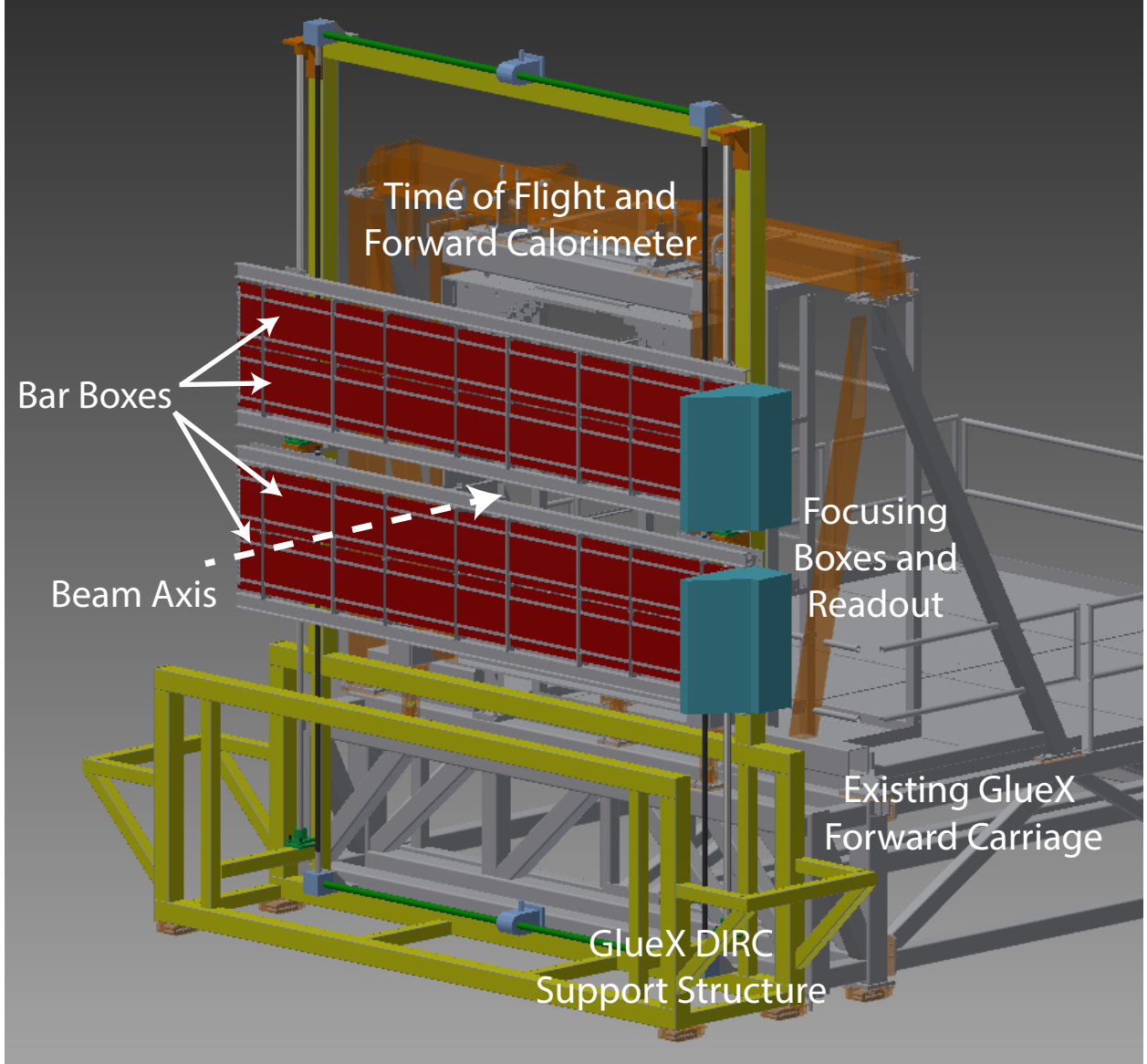


FIG. 42. A conceptual design showing the integration of the DIRC into the GLUEX forward carriage.

box bearing interface, whether it be from I-beam bowing, lateral track misalignment, or another source. The proposed horizontal frame will also allow relatively easy loading of the bar boxes into the support structure.

Bar boxes will be slid in from the side much in the same manner they were loaded into the original BaBar Detector, using similar fixtures. The boxes can be slid opposite the location of the focusing box. The focusing box can then be positioned and oriented. Finally the boxes can be individually slid into the focusing box and fixed in place.

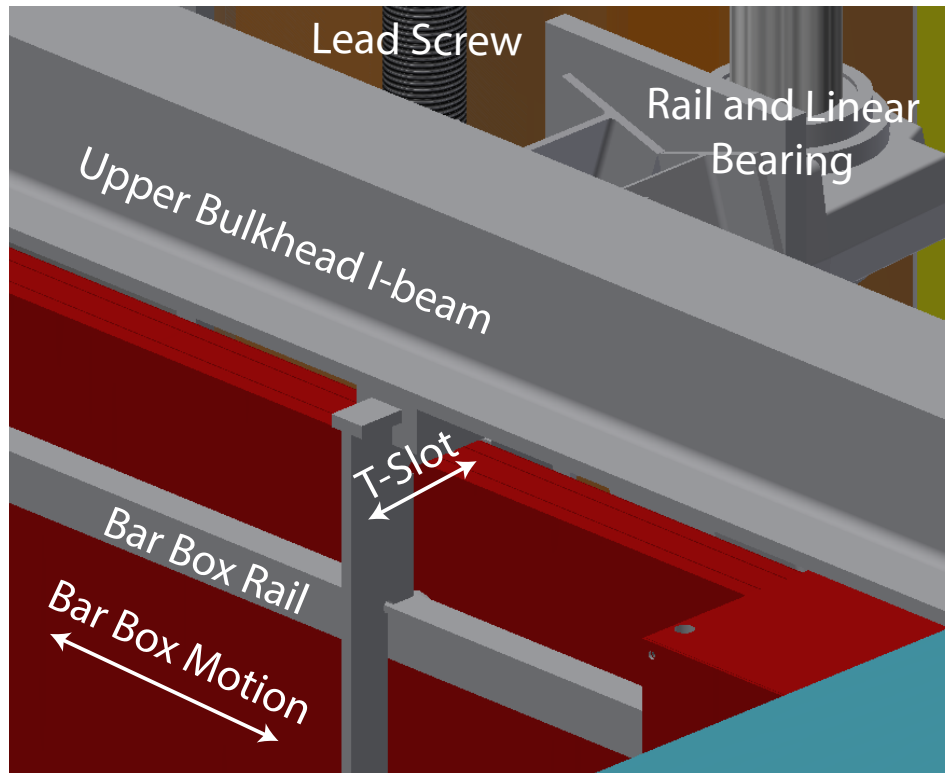


FIG. 43. A detailed view of the box support system, rails, and allowable motion.

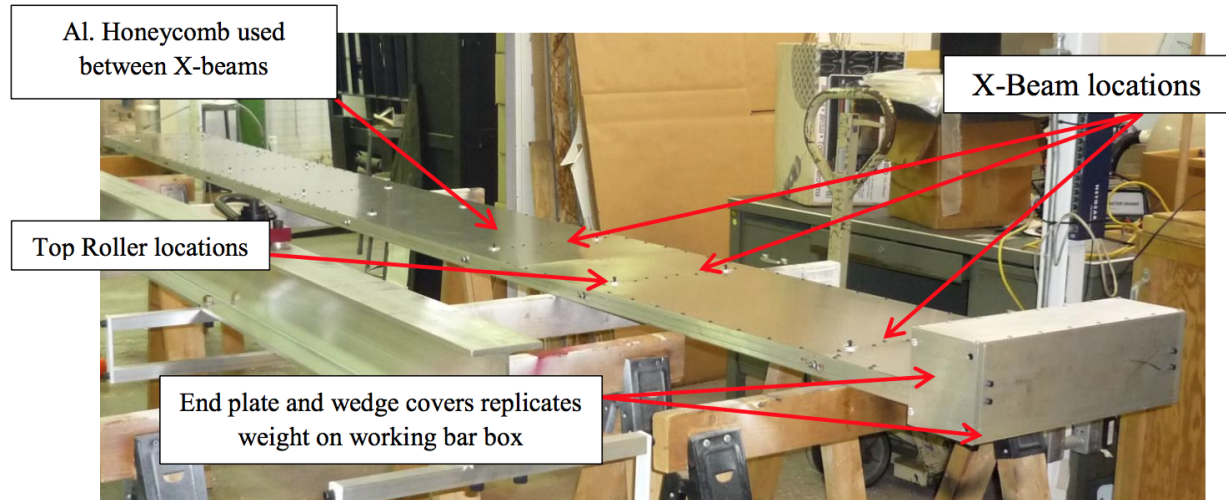


FIG. 44. Photo of the replica bar box that was constructed to match the mechanical dimensions, weight, and moments of an actual bar box.

VII. TRANSPORT TO JLAB

We have had preliminary discussions with Rock-It Cargo, a world-wide shipper of delicate art and industrial equipment regarding coordination of the shipment from SLAC to Jefferson Lab. We plan to transport the bars from SLAC to Jefferson Lab over road via air ride trailer. The trailer will be temperature controlled and equipped with a liquid nitrogen dewar to maintain constant flow of nitrogen through the bar boxes. There is concern that optical joints between bars may be brittle, therefore physical shock should be avoided during transport. In order to develop a crating system for the bar box, we worked with Rock-It's crating subcontractor: Art Crating Los Angeles (ACLA). In addition we constructed a full scale mock bar box that matches the weight and moments of the actual device to use to test the crating system. (See Fig. 44.) ACLA sent a construction manager to Indiana U. for on-site consultation, to view the mock bar box and discuss our needs. After several weeks of communication and construction, ACLA delivered a prototype crate assembly to IU. ACLA factored in the many requirements of the bar box move, and built a high quality crate that is capable of meeting many of the needs. The crate is essentially a "crate within a crate", providing ample rigidity to prevent any flexing along the length of the bar box. Fundamental modes of vibration of the entire box structure are in the neighborhood of 10 Hz, which can be driven by overland transit. Therefore a rigid inner structure is critical to prevent these. The entire assembly can be fully taken apart to make loading and unloading relatively easy using a fixture built from

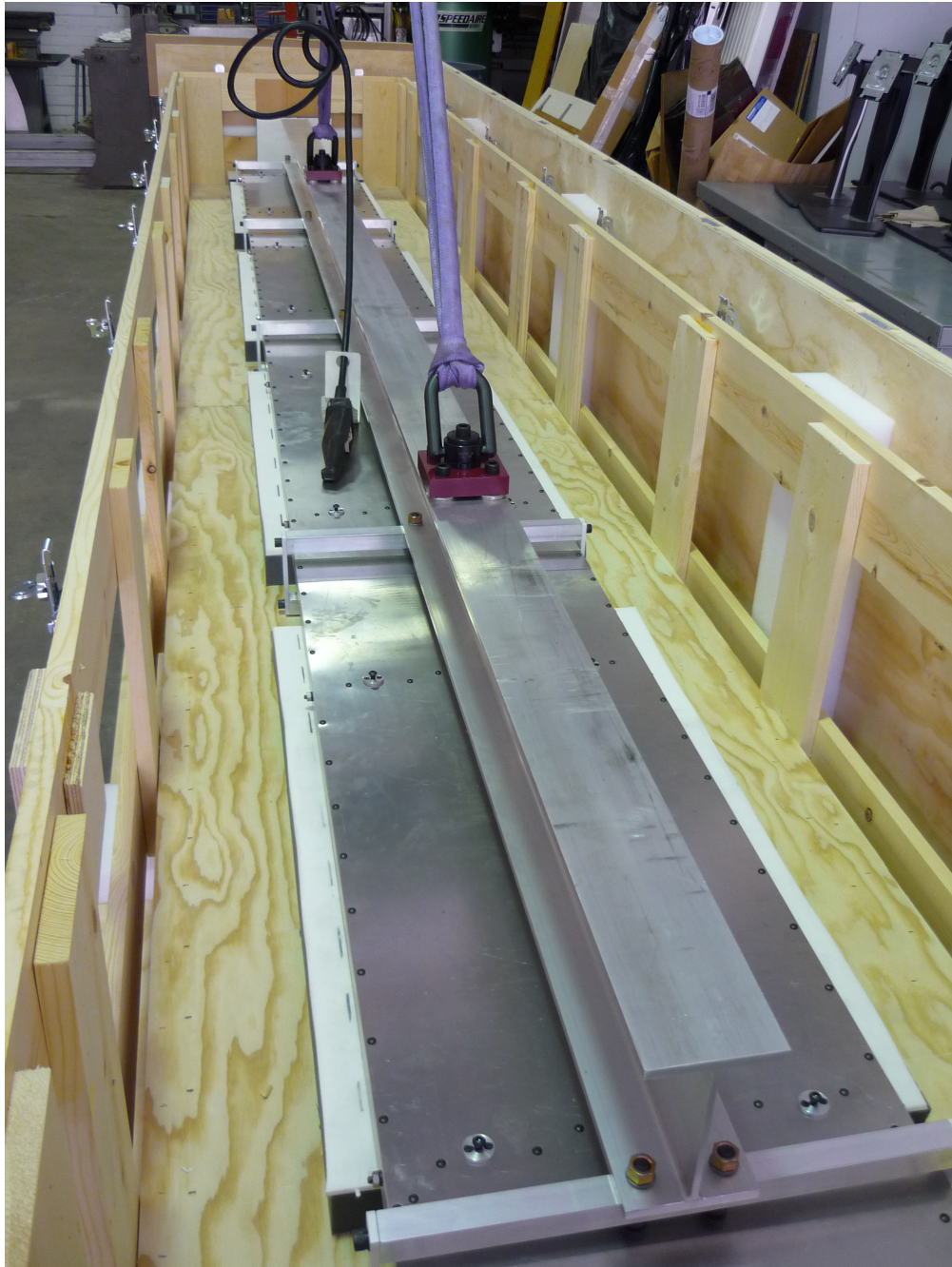


FIG. 45. Photo of loading the mock bar box into the shipping crate utilizing a lifting fixture to prevent flexing the box.

an I-beam to eliminate flexing. (See Fig. 45.) We discuss the performance of this crate below, but first it is appropriate to consider what level of shock may cause damage to the bars.

We begin by using an finite element analysis to estimate the internal stresses assuming that a $3g$

acceleration will be experienced in transit. Assuming the bar box and internal bar support buttons remain rigid, acceleration of the box would cause bending of the bars in between the support buttons. Any elastic compression of the buttons would mitigate this bending. We evaluated the bending stress of a quartz bar assembly when subjected to a $3g$ load in excess of the bar's own weight. Along the length of the bar, which is composed of four bars glued together, the longest unsupported span of bar is 700 mm, while spans containing a glue joint are supported by buttons spaced at 520 mm. A $3g$ uniform acceleration generates a maximum deflection in the long span of 0.0023 inches and a corresponding internal stress of 140 psi, about a factor of 50 below the rupture strength of fused silica. The shorted spans, which contain glue joints, deflect only 0.0004 inches and the internal stress maximum stress in this region is 20 psi. Reference [30] states a tensile strength of epoxy used in the DIRC that exceeds 1000 psi. Even with the consideration that the strength of the epoxy may be degraded due to aging, these estimates suggest at least an order of magnitude safety margin. We therefore aim for a crate design that keeps shock as low as reasonably possible, but consider $3g$ an acceptable limit in dimensions transverse to the axis of the bar.

Accelerations along the axis of the bar have potential to exert a force on the window assuming that the bars slide freely on the buttons. In the static configuration, springs opposite the window exert about 340 lbs. of force on the window, which was designed to keep glue joints in compression under earthquake events and compensate for the hydrostatic load on the window from the BaBar water tank. The weight of the quartz itself inside the box is approximately 200 lbs. The desire to keep the glue joints in compression suggests a limit for axial accelerations of $1.5 g$. In one direction this would not exceed the spring pressure and in the other direction it would result in a load on the window of about 640 lbs. A finite element analysis with 1030 lbs. on the window results in a minimum safety factor of 11.4, indicating that a load of 640 lbs. will not rupture the window. To validate the FEA, a fused silica window with replica flange was tested under a continuous load of 1030 lbs. for a period of two weeks and no damage was observed. Like the transverse direction we would like to keep the acceleration as low as reasonably possible, but consider $1.5 g$ an acceptable limit.

We have conducted preliminary tests of the crate to understand what shock the bar box might experience on the road during transit. We instrumented the mock bar box as well as the inner and outer crates with three-axis accelerometers that record data at 400 Hz. For preliminary testing we raised one end of the crate a couple inches off of a concrete floor and then let the end free fall onto the concrete, an extreme shock. We were able to achieve maximum shock damping by

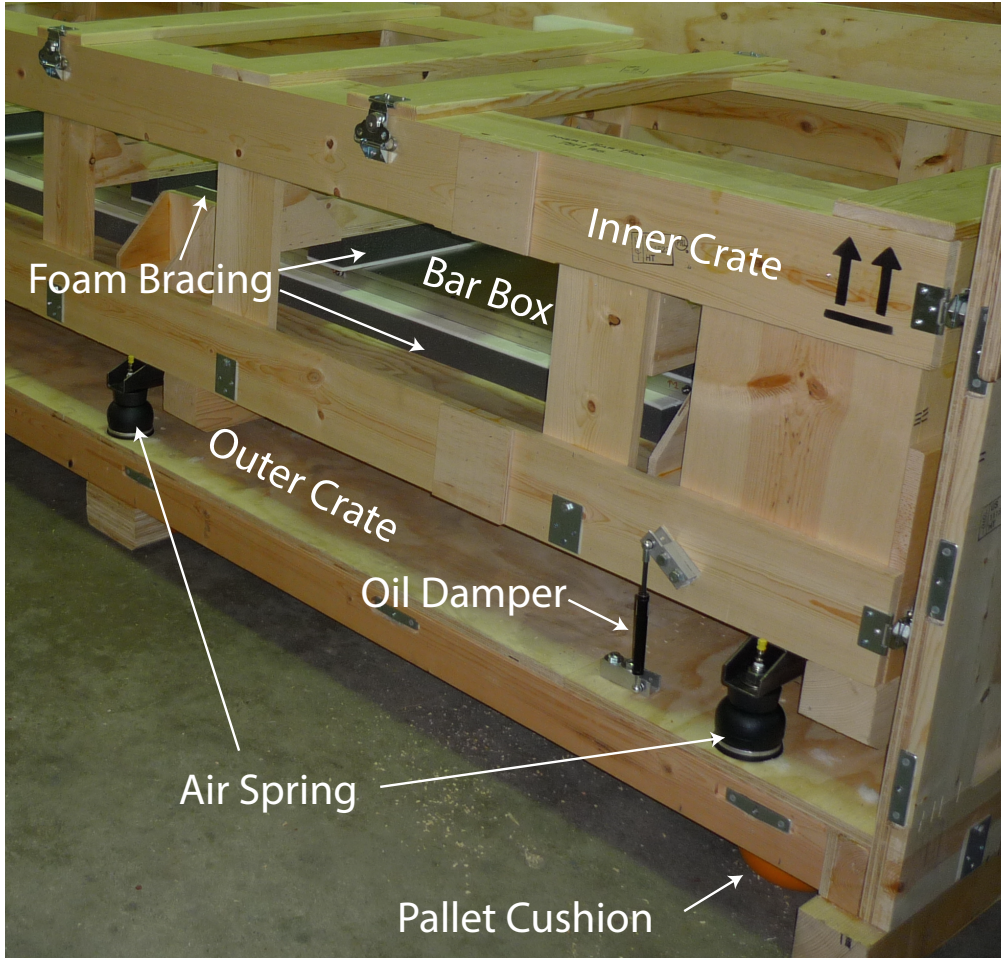


FIG. 46. A photo showing the key shock absorbing components of the shipping crate.

isolating the inner crate from the outer crate using a system of eight air springs. To damp the oscillation introduced by these springs we utilized four variable-strength oil dampers. After optimizing pressures in both systems we were able to attain significant shock reduction. When dropping the crate, accelerometers on the outer crate registered acceleration of $14\ g$ upon impact with the floor while accelerometers on the bar box registered only $2.5\ g$. For the actual transit application we propose plumbing all air springs to common regulated pressure source, e.g., compressed air bottle, to maintain constant pressure in the air springs throughout the trip. A photo showing the proposed crate configuration and key components in Fig. 46.

Additional testing was performed by instrumenting the bar box and crate and loading it onto an air-ride suspension flatbed semi-trailer with a load capacity of 25 tons, a similar configuration to the proposed shipping procedure. Accelerometers were also attached to the trailer bed. The truck

was then driven for four hours on local, state, and interstate highways in southern Indiana. The most extreme acceleration event of the trailer was in the vertical direction and peaked at about $10\ g$. During this event the maximum recorded bar box acceleration was under $2\ g$. Figure 47 shows a sample of accelerometer data for both the trailer and bar box during the test. The crating system attenuates shocks of greater than $6\ g$ to the $1\ g$ level. Vertical oscillation of the truck bed in the 10-20 Hz frequency range, characteristic of wheel balance vibrations in overland transit, is visible and supports the idea that a rigid inner crate that prohibits flexing modes of vibration is essential. Accelerations in the lateral direction can be generated if for example one side of the trailer drops into a hole in the road. The maximum lateral acceleration observed throughout the test was $2.8\ g$, typical values were between $0.5\ g$ and $1.5\ g$. While $2.8\ g$ is below our goal, we plan to reduce this by the addition of air springs in the lateral direction between the top of the inner crate and outer crate. Acceleration fore and aft was typically low, between $0.25\ g$ and $0.40\ g$, with a maximum recorded acceleration of $0.56\ g$, which is below our limit of $1.5\ g$. Naively one expects aft acceleration to be potentially largest in braking events; therefore, we propose to orient the boxes such that the window is to the rear of the trailer to avoid loading the window during a hard braking event.

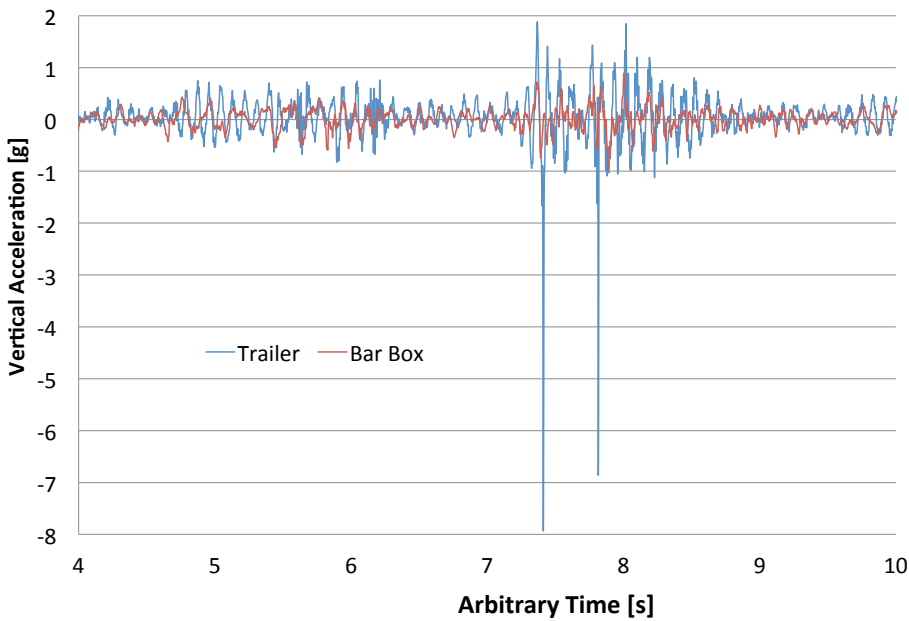


FIG. 47. Vertical acceleration data recorded during simulated shipping test with bar box and crate. Accelerations of both the trailer bed and bar box itself are shown. Large acceleration events such as these are atypical in the full four-hour data set.

VIII. FIRST ARTICLE VALIDATION PLANS

We plan to finalize our mirror-characterization work at MIT/Bates in the next few months. Once this work is complete – and we are confident that the mirrors will meet our needs – we will choose which mirror technology to use in the focusing box, then proceed with finalizing the focusing box design. The boxes will then be built and assembled at MIT/Bates. We believe that the most difficult tasks remaining will then be attaching the focusing boxes to the BaBar DIRC boxes, determining the alignment of the system to $\lesssim 0.5$ mrad precision, and verifying the photon yield.

None of these tasks is easy to study using a prototype, without requiring a huge effort to set up the required tests. Instead we propose the following plan:

- We will construct one of the focusing boxes (Box1) at MIT/Bates. We will then perform all possible testing/validation that can be done at MIT/Bates. This will include aligning/calibrating the mirrors using LEDs and/or lasers, along with filling and leak-testing the box. We plan to fabricate a replica of the end of a BaBar DIRC bar box, so that we can test

the water-tight seal. The type of seal required is the same as successfully implemented at BaBar (bar boxes to water tank). Note that prior to this step, we will have already validated the mirrors themselves.

- Once we are satisfied that Box1 has passed all of the tests we can perform at MIT/Bates, we will ship Box1 to JLab.
- At or before this time, we will have shipped the BaBar DIRC bars to JLab. The support structure for the bar boxes will also need to be in place.
- The BaBar DIRC bar boxes will be installed, and Box1 will be attached to two of them. At this point, we can quickly verify the quality of the seal, and do a rough alignment survey.
- We will instrument some fraction (depending on how many PMTs have been purchased and tested) of Box1, and integrate it into the GLUEX DAQ system. We will then determine the alignment and photon yield of the system *in situ* using GLUEX data.

Preliminary tests performed using simulated GLUEX events suggest that – using a fully-instrumented focusing box – alignment to 1 mrad can be achieved using $\mathcal{O}(1000)$ particles of known identity per degree of freedom. We plan to use copious samples of $K_S \rightarrow \pi^+ \pi^-$ decays, which can be selected with very high purity by the presence of a displaced vertex, to precisely align the system. Other data samples may also be used.

We will then evaluate the performance of Box1. We intend for Box1 to meet our needs and to be part of the final GLUEX FDIRC. However, if these studies using real data reveal any deficiencies, we will take the following steps:

- Consider whether to make any changes to our nominal design prior to building Box2. We do not need Box1 and Box2 to be identical.
- Consider whether to augment Box1. Even if a problem is found, it is likely that Box1 can be augmented cheaply given that most of its components are robust and simple. Only a problem with the mirrors would likely require an expensive augmentation, and we plan to validate the mirrors separately prior to building Box1.

We expect that construction of Box2 can be completed quickly enough that it can be installed approximately half a year after Box1. Therefore, it is likely that following this plan, we can install both Box1 and Box2 by the time that all of the PMTs have been acquired.

IX. PROJECT DETAILS

A complete management plan is being developed as a separate “Program Management” document to be approved by JLab management and DOE, with a detailed description of the management, organization, timeline and budget. In the section below we provide an overview of that document relevant to the technical design report.

A. Institutional contributions

The contributions of the three primary institutions involved in the GLUEX DIRC project are described in Table VII. Recently, the GSI group responsible for the PANDA DIRC has also joined the GLUEX DIRC efforts, providing valuable insights and experience from their prototype development.

TABLE VII. Institutional contributions to the GLUEX DIRC project.

Institution	Contributions
Indiana University	Bar box transport to Jefferson Lab Detector Support Structure
Jefferson Lab	MaPMT Photosensors Electronics and DAQ Installation of DIRC detector in GlueX
MIT	Focusing optics box Optical mirrors Fused silica window

X. SUMMARY

The ability to reconstruct kaon final states is absolutely critical to maximizing the physics potential of the GLUEX experiment. We have developed and presented a design for an FDIRC detector to enhance the particle identification capabilities of GLUEX. The FDIRC utilizes one-third of the quartz bars from the BaBar DIRC, along with the boxes that house the bars. Development of the focusing box and readout systems is well underway. These designs meet the physics requirements, while also minimizing cost and risk.

ACKNOWLEDGEMENTS

We would like to thank J. Va'vra, B. Ratcliff, and B. Wisniewski for their useful discussions and technical information they provided about the BaBar DIRC. We thank M. Benettoni and INFN of Padova for computer models of the BaBar DIRC box.

A. LETTER FROM BABAR REUSE COMMITTEE



July 10, 2014

Matthew Shepherd
Indiana University
Bloomington, IN 47405-7105

Curtis Meyer
Carnegie Mellon University
Pittsburgh, PA 15213

Dear Matt and Curtis:

Several months ago, you and your colleagues submitted a proposal to reuse 4 of the BABAR Fused Silica boxes from the BABAR DIRC. As you know, given that there were multiple requests for these components, as the Director of SLAC PPA and with the support of DOE OHEP, I instituted a formal process to determine how best to deploy these valuable components. A reuse committee was appointed consisting of Brian Meadows, Blair Ratcliff (Chair), Jerry Vavra, and Bill Wisniewski and proposals for redeployment of the DIRC bars were solicited. By this letter, I wish to inform you of the results of that process.

The committee instigated a process comprised of the following elements:

1. As an initial step, an expression of interest from proponents for the reuse of DIRC components was sent by email to the committee chair in November, 2013.
2. A more detailed proposal from proponents was sent by email to the committee chair by December, 2013. Though the proposals were somewhat informal, with no strict lengths or formats defined, we thank the proponents for the efforts they expended to give the clearest possible picture of their intended reuse applications. There were opportunities for questions and responses and other interactions between the committee members and the proponents during this time period. Visits to see the DIRC components at SLAC were encouraged and helped some of the proponents to better understand what would be involved in a given reuse.

3. Based on this input, the expert panel carefully evaluated the suggested reuse options and advised SLAC and the DOE OHEP about the viability of the proponents' plans for reuse and implementation.
4. SLAC then reviewed the proposed reuses with OHEP on multiple occasions, and reached agreement to proceed with the implementation described here.

The committee's review included many considerations, both project specific and more general, including

- Technical feasibility and failure modes?
- Does the reuse involve internal reworking of the boxes or bars?
- Scientific interest and relevance to HEP?
- Support effort required from SLAC, if any?
- DOE-HEP interest and the broader DOE interest?
- SLAC interest and possible involvement?
- Scenarios for reuse; should the boxes go to more than one experiment.

All proposals received described technically credible and scientifically significant reuse options. However, each was unique and cut across the decision making criteria in different ways. Each also had a number of technical challenges and project uncertainties that will require substantial effort to fully address as they go forward. In general, reuse scenarios that required reworking of boxes or bars were strongly deprecated.

Based on the above considerations, the committee made the following comments and recommendations for your GLUEX proposal:

"The primary goal of the GlueX experiment is to search for and study the spectrum of so-called hybrid mesons that are formed by exciting the gluonic field that couples the quarks. The addition of a Cherenkov-based PID system utilizing the BaBar DIRC components will dramatically increase the number of potential hybrid decay modes that GlueX can access and will reduce the experimental backgrounds from misidentified particles in each mode. This enhanced capability will be crucial in order for the GlueX experiment to realize its full discovery potential.

The proposal is the most developed proposal among all submitted in terms of a detailed simulation results and plans for how to use bar boxes. They benefitted greatly from a detailed knowledge of DIRC bar boxes and FDIRC (a detailed computer model was transferred to them), as well as the FDIRC camera MC software package and many discussions with FDIRC group. Therefore they have already implemented a detailed simulation of the FDIRC optics, and are presently attempting to modify it for their application. Specifically, they want to combine four bar boxes into one optical box with a long spherical mirrors in one common oil

bath (the actual optical design is similar to the 1st FDIRC prototype). Removing side reflections is highly desirable in the reconstruction as it avoids introducing ambiguities in the pattern recognition. They consider a FDIRC separated quartz-based camera design as a fall back solution. Though challenging, the project was well thought out. It does not require any internal reworking of the bar box. The physics return from a successful DIRC in GlueX is well worth the effort and supports a program of significant interest to DOE."

Concerns raised by the committee included the following:

- Large area LLAPD MCP detectors may not be available any time soon. In addition, the present LLAPD detectors strip readout may not be suitable for high background.
- Stress on the window when the bar box is oriented vertically may be an issue, although the initial FE analysis study of stresses on the quartz window showed that the vertical design would work.

Based on these recommendations and comments, with the concurrence of DOE, SLAC will provide four bar boxes to GlueX for the program described in your proposal as soon as it can be arranged. We encourage you to begin discussions with appropriate members of the committee as soon as practical to understand how to implement this decision. It should be realized the SLAC has no experience shipping bar boxes offsite, so careful engineering will be needed from you to insure that the boxes make it to you intact. I also understand that the GlueX collaboration may be considering doing a significant amount of additional work at SLAC, including attaching wedges to the bar boxes, before shipping boxes to JLAB. The level of available SLAC support for bar box modifications and related use of SLAC facilities, such as the clean room, will need careful evaluation for feasibility and cost. This work would have obvious implications for the shipping time scale.

It should be noted that there were other competing proposals from ePHENIX and LHCb for use of bar boxes on a longer time scale than GlueX and with unresolved feasibility questions. While we are providing four bar boxes for the full duration of the GlueX program, we do suggest that GlueX remain aware of use possibilities by other experiments at a later time, and attempt to maintain the viability of all bar boxes for the long term.

We apologize that the steps of this decision making process has taken longer than we had hoped. We thank you for your interest in our solicitation, and for thinking about how to take advantage of the opportunities that these bars provide. If you have any questions at all, please get back to me, and/or members of the panel. We sincerely hope that you will be successful in your GlueX DIRC based PID fabrication program and look forward to interacting with you as you put together a final plan for shipping the boxes.



David B. MacFarlane
Professor and Director
Particle Physics and Astrophysics

cc: B. Ratcliff
 W. Wisniewski
 R. Ent
 J. Siegrist
 T. Hallman

B. SUMMARY OF REVIEWS BY JEFFERSON LAB'S PROGRAM ADVISORY COMMITTEE

2012: The GLUEX collaboration submitted a proposal entitled “A study of meson and baryon decays to strange final states with GlueX in Hall D” [1] to Jefferson Lab’s Program Advisory Committee (PAC39). The report from PAC39 conditionally approved this proposal conditional on the final design of the particle ID system [4].

2013: The GLUEX collaboration submitted a proposal entitled “An initial study of mesons and baryons containing strange quarks with GlueX” [2] to Jefferson Lab’s Program Advisory Committee (PAC40). This proposal utilized only the baseline equipment in Hall D (*ie.* no FDIRC) and was approved in the PAC40 report for 200 PAC days of beamtime, the so-called Phase IV running period [5].

2014: The GLUEX collaboration submitted a proposal entitled “A study of decays to strange final states with GlueX in Hall D using components of the BaBar DIRC” [3] to Jefferson Lab’s Program Advisory Committee (PAC42) as a followup to the conditionally approved PAC39 proposal. In addition to the baseline equipment in Hall D this proposal also utilizes the FDIRC and was approved in the PAC42 report (see Appendix C) with an additional 20 PAC days for FDIRC commissioning [6].

C. REPORT FROM JEFFERSON LAB'S 42nd PROGRAM ADVISORY COMMITTEE

C12-12-002

Scientific Rating: A

Recommendation: Approve

Title: **A study of decays to strange final states with GlueX in Hall D using components of the BaBar DIRC**

Spokesperson: Curtis Meyer

Motivation: This proposal is an extension of the already approved GlueX experiments on meson spectroscopy. For the proposed running, the detector system will be crucially extended by adding a forward Cherenkov particle identification system to enable especially kaon identification at high momenta (3σ K/ π separation up to ~ 4 GeV/c). Without such a system the GlueX program cannot be successfully pursued without severe restrictions. Therefore, PAC 40 strongly encouraged the GlueX collaboration to move forward with the design of such a system and aim at an early installation. The mapping of the spectrum of conventional and exotic hadrons will ultimately require the implementation of a dedicated particle ID system in the forward direction. Kaon identification is essential for resolving the flavor composition of meson states and is needed to allow for a systematic (coupled channel) amplitude analysis of many different hadronic final states to be really able to map out the spectrum of hybrid as well as of conventional mesons (addressing e.g. whole exotic multiplets and not only a single state). The planned investigation of cascade baryons will also profit from the new detector capabilities. The proposal was already given conditional approval in PAC39, conditional on the final design of the particle ID system.

Measurement and Feasibility:

The second stage (named stage IV) of the experiment was approved by PAC40 as E12-13-003 (200 days at an average intensity of 5×10^7 tagged photons/s on target), including the implementation of a level-three trigger based on a new computing farm. This running will provide an increase in statistics by a factor 10 over the initial GlueX running. The collaboration showed that this increase in statistics, coupled with a sophisticated multivariate analysis, allows the production of 10^4 events per 10 MeV/c² mass bin while keeping the background contamination within 10%. The PAC40 proposal was based on the baseline GlueX setup only.

With the present proposal, a design of a Cherenkov PID detector for Hall D is put forward, as requested by PAC39 and again strongly encouraged by PAC40. The design is based on the BaBar DIRC bars, which are available to the collaboration. Including the independent DIRC information into the multivariate analysis provides a high discrimination power and significantly improves the purity of the data samples, and therefore their sensitivity on the contributing amplitudes. Purities of 90% reached in simulations without the DIRC can now be pushed to 99% for several final states and to better than 95% in nearly every case. The latter increase would lead to a sensitivity increase of a factor of 2, the former to a factor of 9, which is a large step forward toward a better understanding of the hadron spectrum.

Issues: The design is viable but R&D is still required. It needs to be decided whether the DIRC can be mounted vertically and whether the new technology of micro-channel plates is usable for light detection or whether the more conservative and more expensive solution of multi-anode PMTs needs to be chosen.

The PAC strongly encourages the GlueX-collaboration to work with the JLab Physics Division for an optimization of the FDIRC-readout and the time schedule.

Recommendation: Approve

GlueX is the flagship experiment in Hall D; the physics motivation for the proposed running is very sound. The motivation for the hardware extension is very obvious to reach the physics goals of the experiment and is strongly supported by the PAC.

-
- [1] GLUEX Collaboration, “A study of meson and baryon decays to strange final states with GLUEX in Hall D,” *Presentation to PAC 39*, (2012). Available at: <https://www.jlab.org/exp-prog/proposals/12/PR12-12-002.pdf>
- [2] GLUEX Collaboration, “An initial study of mesons and baryons containing strange quarks with GlueX,” *Presentation to PAC 40*, (2013). Available at: <https://www.jlab.org/exp-prog/proposals/13/PR12-13-003.pdf>
- [3] GLUEX Collaboration, “A study of decays to strange final states with GlueX in Hall D using components of the BaBar DIRC,” *Presentation to PAC 42*, (2014). Available at: <https://www.jlab.org/exp-prog/proposals/14/C12-12-002.pdf>
- [4] Report from Jefferson Lab’s 39th Program Advisory Committee. Available at: https://www.jlab.org/exp-prog/PACpage/PAC39/PAC39_Final_Report.pdf
- [5] Report from Jefferson Lab’s 40th Program Advisory Committee. Available at: https://www.jlab.org/exp-prog/PACpage/PAC40/PAC40_Final_Report.pdf
- [6] Report from Jefferson Lab’s 42nd Program Advisory Committee. Available at: https://www.jlab.org/exp-prog/PACpage/PAC42/PAC42_FINAL_Report.pdf
- [7] J. J. Dudek, Phys. Rev. D **84**, 074023 (2011).
- [8] J. J. Dudek, R. G. Edwards, M. J. Peardon, D. G. Richards and C. E. Thomas, Phys. Rev. Lett. **103**, 262001 (2009).
- [9] J. J. Dudek, R. G. Edwards, M. J. Peardon, D. G. Richards and C. E. Thomas, Phys. Rev. D **82**, 034508 (2010).
- [10] J. J. Dudek, R. G. Edwards, B. Joo, M. J. Peardon, D. G. Richards and C. E. Thomas, Phys. Rev. D **83**, 111502 (2011).
- [11] R. G. Edwards, J. J. Dudek, D. G. Richards and S. J. Wallace, Phys. Rev. D **84**, 074508 (2011).
- [12] J. Beringer *et al.* [Particle Data Group Collaboration], Phys. Rev. D **86**, 010001 (2012).
- [13] C. A. Meyer and Y. Van Haarlem, Phys. Rev. C **82**, 025208 (2010).
- [14] M. Ablikim *et al.* [BES Collaboration], Phys. Rev. Lett. **100**, 102003 (2008).
- [15] B. Aubert *et al.* [BABAR Collaboration], Phys. Rev. D **74**, 091103 (2006).
- [16] C. P. Shen *et al.* [Belle Collaboration], Phys. Rev. D **80**, 031101 (2009).
- [17] B. Aubert *et al.* [BABAR Collaboration], Phys. Rev. Lett. **95**, 142001 (2005).
- [18] T. E. Coan *et al.* [CLEO Collaboration], Phys. Rev. Lett. **96**, 162003 (2006).
- [19] Q. He *et al.* [CLEO Collaboration], Phys. Rev. D **74**, 091104 (2006).
- [20] C. Z. Yuan *et al.* [Belle Collaboration], Phys. Rev. Lett. **99**, 182004 (2007).
- [21] F. E. Close and P. R. Page, Phys. Lett. B **628**, 215 (2005).
- [22] S. -L. Zhu, Phys. Lett. B **625**, 212 (2005).

- [23] E. Kou and O. Pene, Phys. Lett. B **631**, 164 (2005).
- [24] X. -Q. Luo and Y. Liu, Phys. Rev. D **74**, 034502 (2006) [Erratum-ibid. D **74**, 039902 (2006)].
- [25] G. -J. Ding and M. -L. Yan, Phys. Lett. B **657**, 49 (2007).
- [26] P. R. Page, E. S. Swanson and A. P. Szczepaniak, Phys. Rev. D **59**, 034016 (1999).
- [27] N. Isgur, R. Kokoski and J. E. Paton, Phys. Rev. Lett. **54**, 869 (1985).
- [28] GLUEX Collaboration, “Mapping the Spectrum of Light Quark Mesons and Gluonic Excitations with Linearly Polarized Protons,” *Presentation to PAC 30*, (2006). Available at: http://www.gluex.org/docs/pac30_proposal.pdf
- [29] GLUEX Collaboration, “The GLUEX Experiment in Hall D,” *Presentation to PAC 36*, (2010). Available at: http://www.gluex.org/docs/pac36_update.pdf
- [30] I. Adam *et al.*, Nucl. Instr. and Meth. **A538**, 281 (2005).
- [31] C. Field *et al.*, Nucl. Instr. and Meth. **A553**, 96 (2005).
- [32] C. Field *et al.*, Nucl. Instr. and Meth. **A518**, 565 (2004).
- [33] J.F. Benitez *et al.*, Development of a focusing DIRC, IEEE Nuclear Science Conference Record, October 29, SLAC-PUB-12236 (2006).
- [34] J. Va’vra *et al.*, The Focusing DIRC- the First RICH Detector to Correct the Chromatic Error by Timing, Presented at Vienna Conference on Instrumentation, February, SLAC-PUB-12803 (2007).
- [35] J.F. Benitez *et al.*, Nucl. Instr. and Meth. **A595**, 104 (2008).
- [36] J. Va’vra *et al.*, Nucl. Instr. and Meth. **A718**, 541(2013).
- [37] LAPPD Collaboration, “The Development of Large-Area Fast photo-detectors”, Proposal to the Department of Energy’s Office of High Energy Physics (2009).
- [38] F. Gargano *et al.*, Nucl. Instr. and Meth. **A718**, 563 (2013).
- [39] S.P. Malace, B.D. Sawatzky, H. Gao, JINST **8**, P09004 (2013).
- [40] R.A. Montgomery *et al.*, Nucl. Instr. and Meth. **A695**, 326 (2012).
- [41] R. A. Montgomery *et al.*, Nucl. Instrum. Meth. A **790**, 28 (2015) [arXiv:1409.3622].
- [42] M. Calvi, P. Carniti, L. Cassina, C. Gotti, M. Maino, C. Matteuzzi and G. Pessina, [arXiv:1506.04302]
- .
- [43] Hamamatsu Photonics K. K., “Multianode PMT Assembly H8500/H10966 Series”, http://www.hamamatsu.com/resources/pdf/etd/H8500_H10966 TPMH1327E02.pdf
- [44] Hamamatsu Photonics K. K., “Multianode PMT Assembly H9500, H9500-03”, http://www.hamamatsu.com/resources/pdf/etd/H9500_H9500-03 TPMH1309E01.pdf
- [45] Hamamatsu Photonics K. K., “Multianode PMT Assembly H12700”, <https://www.hamamatsu.com/resources/pdf/etd/H12700 TPMH1348E.pdf>
- [46] Ardavan Ghassemi, Technical Sales Rep for Scientific Projects, Hamamatsu Photonics K. K., Private Communication
- [47] <http://www.seliteskudotech.it>

- [48] Y. Qiang, C. Zorn, F. Barbosa and E. Smith, “Radiation Hardness Tests of SiPMs for the JLab Hall D Barrel Calorimeter,” Nucl. Instrum. Meth. A **698**, 234 (2013), arXiv:1207.3743 [physics.ins-det], https://halldweb.jlab.org/wiki/index.php/SiPM_Radiation_Hardness_Test
- [49] <http://www.eljentechology.com/index.php/products/accessories/94-ej-550>
- [50] B. Raydo, Jefferson Lab Fast Electronics Group, Private Communication
- [51] M. Contalbrigo, E. Cisbani, P. Rossi, Nucl. Instr. and Meth. **A639**, 302 (2011).
- [52] CLAS12 Collaboration, RICH Technical Design Report (2013).
- [53] S. Blin *et al.*, “A generic photomultiplier readout chip”, JINST **5**, C12007 (2010).
- [54] B. Raydo, “Sub-System Processor Manual”, https://coda.jlab.org/wiki/Downloads/HardwareManual/SSP/SSP_Module_HallD.pdf, (2009).
- [55] M. Contalbrigo talk at CLAS12 RICH internal review, June 2015.
- [56] L. Brieman *et al.*, *Classification and regression trees*, Wadsworth International Group, Belmont, California (1984).
- [57] B.P. Roe *et al.*, Nucl. Instr. and Meth. **A543**, 577 (2005).
- [58] A. Hoecker, P. Speckmayer, J. Stelzer, J. Therhaag, E. von Toerne, and H. Voss, *TMVA: Toolkit for Multivariate Data Analysis*, PoS A CAT 040 (2007).
- [59] B. Thomas *et al.*, arXiv:1105.5409 [physics.ins-det] (2011).